Maritime Moving Target Long Time Integration for GNSS-Based Passive Bistatic Radar

DEBORA PASTINA
FABRIZIO SANTI
FEDERICA PIERALICE
University of Rome "La Sapienza," Rome, Italy

MARTA BUCCIARELLI
Sympas S.r.l., Rome, Italy

HUI MA
DIMITRIOS TZAGKAS
MICHAIL ANTONIOU
MIKHAIL CHERNIAKOV
University of Birmingham, Birmingham, U.K.

This paper addresses the exploitation of Global Navigation Satellite Systems (GNSS) as transmitters of opportunity in passive bistatic radar systems for maritime surveillance. The main limitation of this technology is the restricted power budget provided by navigation satellites, which makes it necessary to define innovative moving target detection techniques specifically tailored for the system under consideration. To this aim, this paper puts forward long integration time techniques able to collect the signal energy over long time intervals (tens of seconds), allowing the retrieval of suitable levels of signal-to-disturbance ratios for detection purposes. A local plane based technique is first considered, providing target detection in a plane that represents the section of maritime area covered by the radar antenna. As a suboptimum solution in terms of achievable integration gain, but more efficient from a computational point of view, a second technique is considered working in the conventional bistatic range and Doppler plane (basic plane based). Results against synthetic and experimental datasets show the effectiveness of the proposed techniques.

Authors' addresses: D. Pastina, F. Santi, and F. Pieralice are with the Department of Information Engineering, Electronics and Telecommunications, University of Rome "La Sapienza," Rome 00184, Italy E-mail: (debora.pastina@uniroma1.it; santi@diet.uniroma1.it; federica.pieralice@uniroma1.it); M. Bucciarelli is with the Sympas S.r.l., Rome 00192, Italy E-mail: (bucciarelli@sympas-srl.it); H. Ma, D. Tzagkas, M. Antoniou, and M. Cherniakov are with the School of Electronic, Electrical and System Engineering, University of Birmingham, Birmingham B15 2TT, U.K. E-mail: (h.ma@xidian.edu.cn; DXT206@student.bham.ac.uk; m.antoniou@bham.ac.uk; m.cherniaokv@bham.ac.uk). *(Corresponding author: Fabrizio Santi.)*

I. INTRODUCTION

Motivated by the well-known benefits of passive radars, over the last years the radar community put a lot of effort in investigating how to exploit existing transmissions to increase the levels of safety and security in the maritime domain. Indeed, the lack of a dedicated transmitter makes such systems inherently low cost, since only the receiver has to be developed. Moreover, they are much lighter than active systems and, hence, can be deployed in places where heavy active sensors cannot be installed, such as marine protected areas. As they do not transmit any signals, they allow covert operations, they are largely immune to jamming and, since the system is intrinsically bistatic, they can represent an effective antistealth defense option. Different kinds of terrestrial illuminators of opportunity have been proved to be able to increase safeguarding maritime security such as GSM [1] and WiMAX base stations [2]. One of the most promising passive radar technologies in this field considers the Digital Video Broadcasting-Terrestrial transmitters [3]. These sources offer a sufficiently high transmitted power allowing very long detection ranges and the potential of these illuminators to monitor maritime traffic has been proved at both theoretical and experimental levels. Nevertheless, terrestrial-based illuminators of opportunity cannot guarantee a global coverage, as for instance in open sea.

The coverage of offshore, open sea areas can be obtained by switching to passive radar systems based on opportunistic satellite transmitters as the Global Navigation Satellite Systems (GNSS) or the many commercial communication satellites in geostationary/geosynchronous orbits (as, for example, for digital television broadcasting). Suitable GNSS candidates can be the Global Positioning System (GPS) [4], the GLObal NAvigation Satellite System (GLONASS) [5], Beidou [6], or the new European Galileo constellation [7]. From a passive radar perspective, GNSS signals are particularly attractive. First, the radar user has full knowledge of the transmitted waveform, which is also optimized for remote synchronization. Moreover, they offer a relatively large signal bandwidth, with a maximum range resolution of 15 m (using Galileo E5a/b signals or the GPS L5), which is a suitable value in the framework of the maritime surveillance. Noticeably, with respect to commercial communication satellites, GNSS offers a unique combination among global coverage, complete reliability, and spatial/waveform diversity. Indeed, GNSS signals are available over the entire earth's surface, even at the poles. Spatial diversity is obtained thanks to the availability of multiple satellites simultaneously illuminating the same area from different angles: typically, 6–8 satellites are made available by the single GNSS constellation so that up to 32

satellites could be exploited when all four GNSS systems will be operative. Waveform diversity is obtained thanks to the transmission of different signals (even in different frequency bands) from the single satellite. Remarkably, both spatial and waveform diversity can be captured by a single receiver inherently providing a multistatic radar system where multiple signals could be combined to increase the performance.

The above-mentioned features of GNSS constellations, along with the highly time precise nature of the transmitted signals, stimulated their alternative utilizations for remote sensing purposes since more than two decades [8]. The analysis of the GNSS reflected signals [GNSS-Reflectometry (GNSS-R)] has brought to a number of well-established technologies to remotely sense the atmosphere and ionosphere, ocean, land surface, and cryosphere [9], [10]. In the field of radar sensors, the exploitation of GNSS signals has been investigated from several years for passive synthetic aperture radar imaging [11]–[18], with the ultimate goal to achieve persistent local area monitoring. With specific regard to surveillance purposes, some studies have been conducted for the detection of aerial targets [19]–[21], whereas only few investigations have been carried out for maritime surveillance purposes. In particular, the feasibility to use GNSS signals has been investigated in [22] considering GNSS-R technology. Concerning radar technologies, in [23], the feasibility of maritime target detection has been investigated using GPS signals with specific reference to a configuration comprising transmitter, airborne receiver, and target aligned on the same direction so that a monostatic behavior of the target can be assumed. The reported results provided a theoretical confirmation of the results in [24] where some experimental evidence of the detectability of a stationary target by means of GPS signal was given.

The first experimental confirmation of the feasibility of GNSS reflected signals acquisition to detect maritime targets in general bistatic geometries was given in [25]–[27]: Particularly, the feasibility was demonstrated against a large target and some appropriate basic signal processing techniques were also provided. This forecasts new studies and experimentations in order to fully exploit the potentials of this technology.

The major issue in using GNSS satellites as illuminators of opportunity is the very low level of electromagnetic (e.m.) field reaching the earth's surface [28], which makes conventional techniques used for target detection inside terrestrial based passive radar systems not directly applicable to the GNSS-based passive radar. To counteract the low level of signal to disturbance ratio in input at the receiver, target energy should be integrated over long integration times. One of the main issues arising with the increase of the integration time is the migration of the target through the resolution cells, which needs to be compensated to do not compromise the detectability of the target. To extend the coherent processing interval (CPI) in the spite of the migration of the moving target through the resolution cells, a number of methods have been proposed, such as the Radon Fourier transform [29], the Radon fractional Fourier transform [30], and the stretch processing [31]. However, it will be shown that the GNSS-passive radar may require integration times that can be up to several tens of seconds. Such long integration times are fundamentally possible due to GNSS coverage, but their exploitation implies the need of techniques tailored for the case of interest. Particularly, it should be noted that a full coherent integration as in [29]–[31] is not feasible over such long dwells, and therefore, we need to resort to hybrid coherent/noncoherent integration of the received signal. A preliminary long integration time technique for the GNSS-based passive radar was proposed in [26] and [27] while, referring to a generic space based passive radar, a fractional Fourier transform based approach was considered in [32].

In this paper, we continue the work in [25]–[27] from both a theoretical and experimental point of view. Particularly, we theoretically demonstrate the need of very long integration times (in the order of several tens of seconds) for detection purposes and we introduce a new technique able to integrate the target returns over long time intervals (in the order of several tens of seconds) and working in the spatial plane representing the section of the maritime area covered by the radar antenna (i.e., local plane). To cope with the long integration time, the technique adopts a multistage approach, comprising a coherent integration inside shorter intervals (named frames), and a noncoherent integration of the frames in the integration window, and compensates the migration of the target returns occurring inside the frame (intraframe) and among the different frames (interframes). Some very preliminary results along this line were reported in [33]. As a suboptimum solution in terms of achievable integration gain, but more efficient from a computational point of view, also a second technique is proposed that works in the basic plane and properly generalizes results in [26] and [27]. Particularly, the generalization consists in: first, the consideration and compensation of the target migration at both intraframe and interframes level (in contrast to [26], [27] where only interframes migration was considered) to possibly increase frame length; second, in changing the order of the different processing steps required for migration compensation to reduce the computational load. For both local and basic plane approaches the adaptation to the unknown target motion conditions is obtained by resorting to proper banks, being each branch in bank matched to a specific motion: to allow the design of the bank, specific criteria are analytically derived and provided for both cases. The performance of the two proposed techniques is first investigated from a theoretical point of view discussing and comparing their advantages and drawbacks: specific focus is on the analysis of the achievable integration gain and of their behavior with respect to the ambiguous detections due to the use of the bank. To support the theoretical investigations, results from experimental campaigns are reported and discussed as well. It is worth to highlight here that the design of a dedicated GNSS-based radar system, specifically tailored for maritime detection, is not currently available, and therefore, for the experimental purposes scientific equipment has been used. As such,
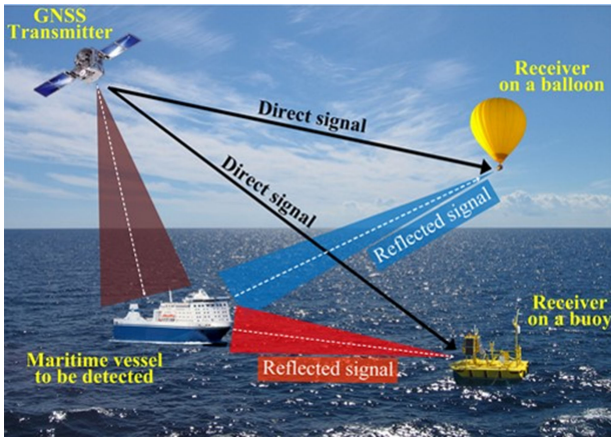
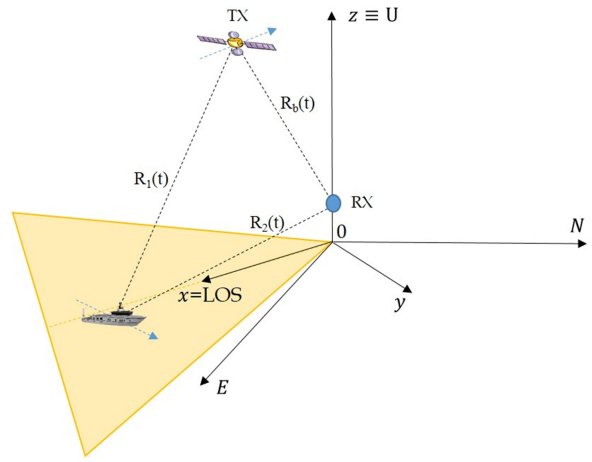Fig. 1. System concept for GNSS-based radar for maritime surveillance.

Fig. 2. System geometry.

reported results aim at showing the relative improvement in SNR and detection range between conventional, short integration time techniques, and the ones proposed here, rather than the absolute SNR and detection range expected from a GNSS-based radar system employing the proposed techniques. In the same sense, the algorithms described here are not only applicable to GNSS but to any bistatic radar system with a restricted power budget. In this frame, two experimental trials have been conducted: the first one (using GLONASS transmitter) involved a small cooperative fishing boat equipped with GPS to provide an accurate reference ground truth for performance analysis and comparison; the second one (using Galileo transmitter) involved multiple opportunity targets with different size following arbitrary trajectories with reference ground truth provided by the automatic identification system (AIS) receiver used in the acquisitions. Obtained results against experimental data prove the feasibility of the conceived system and the effectiveness of the proposed techniques.

The remaining content of this paper is organized as follows. Section II gives an overview of the GNSS-based passive radar in terms of system geometry, link budget, and the target model over considerably long dwell times. Section III describes the proposed long time integration techniques for both cases of local and basic plane and derives the criteria required for the design of the corresponding filter banks. Results against synthetic data are provided in Section IV where different study cases are considered, the two approaches compared, and their advantages and drawbacks discussed, while Section V reports the results achieved by processing the data acquired in the experimental campaigns. Finally, conclusion in Section VI closes the paper.

II. SYSTEM OVERVIEW

The system considered in this paper comprises a GNSS transmitter and a parasitic receiver in a remote location above the sea (see for instance Fig. 1). The receiver is equipped with two RF channels. The former (referred to as reference channel) uses a low-gain antenna pointed toward the sky to record the direct signals from GNSS satellites,

whereas the latter (surveillance channel) employs a higher-gain antenna pointed toward the sea area to be surveyed and collecting the resulting signal reflections. Since GNSS operate on frequency or code division approaches, the receiver can separate the signals emitted by different sources, and each bistatic link can be separately processed. Hereinafter, we consider a scenario comprising a single GNSS transmitter and a stationary receiver.

A. System Acquisition Geometry

The overall system geometry is sketched in Fig. 2 showing the (O, x, y, z) Cartesian reference system, which is obtained as a rotation of the east–north–up reference system making the x-axis coinciding with the projection on the ground plane (x, y) of the pointing direction of the surveillance antenna. Without loss of generality, we assume the origin of the reference system on the projection onto the ground plane (x, y) of the receiver position. Within this local reference we define the parameters describing the trajectories of the transmitter (TX) and of the moving target (TgT) as observed by the stationary receiver (RX) during the observation time T.

Let $t_x(t)$, r_x, and $p(t)$ denote, respectively, the TX, RX, and TgT instantaneous positions at time t within the interval $[-\frac{T}{2}, \frac{T}{2}]$. The trajectory of the transmitter, which is well known and predictable, is obtained as a function of the TX position p_{TX}^0 at $t = 0$, of the TX velocity vector v_{TX} and of the TX acceleration vector a_{TX}, while for the stationary receiver, we have $r_x \equiv p_{RX}$. The ship target moves within the antenna footprint: to derive the geometrical model, we assume the target modeled as a single point-like target. The trajectory of the target is obtained as a function of its position p_{TgT}^0 at $t = 0$, velocity vector v_{TgT}, and acceleration vector a_{TgT}. The instantaneous distances between satellite, receiver, and target are defined as follows: $R_1(t) = |t_x(t) - p(t)|$ is the TX–TgT distance, $R_2(t) = |p(t) - r_x|$ is the TgT–RX distance, and finally $R_b(t) = |t_x(t) - r_x|$ is the TX–RX baseline. Since in the passive radar systems range compression is achieved by matched filtering with a reference signal compensating the

instantaneous delay between transmitter and receiver, the bistatic range history of the target is given by

$$R(t) = R_1(t) + R_2(t) - R_b(t) \quad (1)$$

and its Doppler frequency is obtained as

$$f_d(t) = -\frac{1}{\lambda}\dot{R}(t) \quad (2)$$

being λ the central wavelength associated to the exploited signal.

B. System Link Budget

A basic performance analysis is included here to highlight some key characteristics of the considered system. Particularly, performance is investigated in terms of achievable maximum radar range as a function of the overall available dwell time for assigned false alarm rate and detection probability levels. The analysis is carried out under the following assumptions [28]:

1) noise limited performance;
2) input signal to noise power ratio value does not change in the considered observation time;
3) Swerling 0 target model.

Concerning the target model, it is worth to recall that the Swerling 0 indicates a constant target cross section not fluctuating inside the considered dwell time, which is a bold assumption. However, for performance evaluation, the dwell time is divided in N_f frames of duration T_f: Coherent integration is assumed inside the single frame while noncoherent integration is considered among the N_f frames. This implies that target radar cross section (RCS) needs to be constant inside the frame while frame-to-frame variations can be tolerated. Since Swerling II performance is close to Swerling 0 when integrating a high number of measurements, the derived performance can be regarded also as representative of situations involving a fluctuating target cross section whose amplitude follows a Rayleigh distribution with rate of change in the same order of frame duration.

We denote by $(SNR)_{NCI}$ the signal to noise power ratio (SNR) required to achieve a specific detection probability P_d given a desired false alarm rate P_{fa} when N_f frames are noncoherently integrated: The signal to noise power ratio at the single frame level, SNR_f, needed to achieve the desired performance is related to $(SNR)_{NCI}$ by

$$(SNR)_{NCI} = SNR_f \cdot I(N_f) \quad (3)$$

where $I(N_f)$ is the noncoherent integration improvement factor. For the square-law detector, we can be approximate $I(N_f)$ by means of the following empirical formula:

$$I(N_f)\big|_{dB} = 6.79(1 + 0.253P_d)\left[1 + \frac{\log_{10}(1/P_{fa})}{46.6}\right]$$
$$(\log_{10}N_f)(1 - 0.14\log_{10}N_f$$
$$+ 0.0183\log_{10}^2 N_f) \quad (4)$$

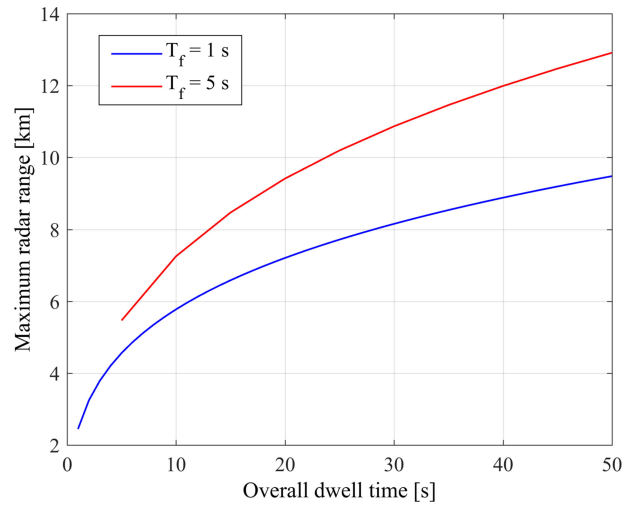
Fig. 3. Maximum radar range as a function of overall integration time.

which is accurate to within about 0.8 dB over a range of about 1–100 for N_f, 0.5–0.999 for P_d, and 10^{-10} to 10^{-2} for P_{fa} [34].

The value of the signal to noise power ratio for the nonfluctuating target detection problem to achieve the desired P_d and P_{fa} can be evaluated by means of Albersheim's equation [35]

$$SNR_f = A + 0.12AB + 1.7B \quad \text{where} \quad A = \ln\frac{0.62}{P_{fa}}$$
$$B = \ln\frac{P_D}{1 - P_D}. \quad (5)$$

Finally, the signal to noise power ratio at frame level can be evaluated as

$$SNR_f = SNR_{input} \cdot T_f B \quad (6)$$

where SNR_{input} is defined as $SNR_{input} = \frac{P_{Rx}}{P_{Noise}}$ being $P_{Rx} = \frac{P_{DenGnd} \cdot \sigma}{4\pi R_2^2 L} A_{Rx}$ the power of the target returns and $P_{Noise} = kT_0FB$ the disturbance noise power. In the previous relations: P_{DenGnd} represents the power density reaching the target (W/m²) evaluated from the minimum power level received on the ground by a 0 dBi receiving antenna as specified by Galileo standard [7], σ denotes the target RCS, A_{Rx} denotes the effective area of the surveillance antenna, L denotes the system losses, k denotes the Boltzman constant, T_0 denotes the standard temperature, F denotes the receiver noise figure, and B denotes the exploited bandwidth. Fig. 3 shows the maximum radar range for $P_{fa} = 10^{-3}$ and $P_d = 0.75$ as a function of the overall dwell time for a target with 30 dBm² RCS and for two values of the frame duration T_f ($T_f = 1$ s, so that a maximum of 50 frames are noncoherently integrated, and $T_f = 5$ s, so that a maximum of ten frames are integrated), for a receiving system whose parameters are similar to those used for experimentation (see Section V) and reported in Table I. From the figure, it can be verified that the achievement of appreciable performance generally requires the integration of the target returns over long time intervals up to several tens of

Parameter	Value	unit
Surveillance antenna area	0.195	m²
Antenna aperture efficiency	0.7	-
Noise figure	1.5	dB
Operating bandwidth	10.230	MHz
System losses	2	dB

seconds. Obviously, such integration requires the definition of suitable target models introduced in the following section.

C. Target Model and Time Constraints

Aiming at performing an integration of the received data for detection purposes, it is of interest to analyze the impact of target motion on the target phase history to analytically derive the time constraints for selecting an appropriate model for the received signal phase. To this purpose, the phase of the received signal is approximated in Taylor series (around $t = 0$) as follows:

$$\phi(t) \approx -\frac{2\pi}{\lambda}\left\{R(0) + \alpha t + \frac{1}{2}\beta t^2 + \frac{1}{6}\gamma t^3 + \frac{1}{24}\delta t^4\right\}$$
$$(7)$$

where the coefficients α, β, γ, δ can be expressed as a function of the kinematic parameters described above (see Section II-A). Based on the criterion that higher order terms of the phase can be neglected if they give rise to a phase variation during the CPI less than $\pi/4$, two fundamental constraints can be derived related to T_{lin} and T_{quad}. The former defines the maximum CPI for which the phase in (7) can be considered as linear: since this infers a constant Doppler frequency, for CPI values lower than T_{lin}, the coherent integration can be realized by means of a Fourier transform; the latter defines the maximum CPI for which the phase in (7) can be considered as quadratic: if the inequalities $T_{\text{lin}} < \text{CPI} < T_{\text{quad}}$ hold, in the coherent integration the Doppler rate has to be compensated by means of dechirping-like methods. For CPI values greater than T_{quad}, more sophisticated phase compensation methods should be taken into account. Nevertheless, as it will be shown ahead, T_{quad} is often greater than values of common interest for the CPI in most practical situations. In order to evaluate T_{lin} and T_{quad}, the upper bounds T_2, T_3, and T_4 related to second-, third-, and fourth-order terms are first derived as

$$\frac{2\pi}{\lambda}|\beta|\frac{t^2}{2}\bigg|_{t=\frac{T_2}{2}} \leq \frac{\pi}{4} \rightarrow T_2 = \sqrt{T_2 = \frac{\lambda}{|\beta|}}$$

$$\frac{4\pi}{\lambda}|\gamma|\frac{t^3}{6}\bigg|_{t=\frac{T_3}{2}} \leq \frac{\pi}{4} \rightarrow T_3 = \sqrt[3]{\frac{3\lambda}{|\gamma|}}$$

$$\frac{2\pi}{\lambda}|\delta|\frac{t^4}{24}\bigg|_{t=\frac{T_4}{2}} \leq \frac{\pi}{4} \rightarrow T_4 = \sqrt[4]{\frac{48\lambda}{|\delta|}}.$$
$$(8)$$

Accounting for typical operating conditions, we can consider that order terms higher than the quartic one give

rise to negligible phase variations. Also, as it will be shown further, in every practical situation it always results in $T_2 < (T_3, T_4)$, whereas depending on target position and velocity, it may result in $T_3 > T_4$ or the other way; therefore, we can write

$$T_{\text{lin}} = T_2$$
$$T_{\text{quad}} = \min[T_3, T_4].$$
$$(9)$$

Table II shows the values of T_{lin} and T_{quad} as a function of the target distance (from RX) at aperture center for different constant target velocities and directions θ (measured clockwise from y-axis), thus referring to the case of a not maneuvering target such as a ship in the open sea. For the shown results, the same configuration of TX–RX described in Section IV has been used. From Table II, we can observe the following.

1) Strict limitations on T_{lin} (and T_{quad}) arise for those targets having a not negligible cross-range velocity component (with respect to receiver LOS) while for targets moving radially a linear approximation suffices.
2) The constraints become more strict as the target speed increases and the distance from the receiver decreases.
3) The linear approximation could be not sufficient to allow the coherent integration of the target returns over a time interval of few seconds that requires a second order approximation.

The above-mentioned constraints will be used in the following to set the CPI value used in both the local and basic plane techniques.

III. MARITIME MOVING TARGET DETECTION TECHNIQUES

The complete processing chain, sketched in Fig. 4, aims at performing the integration over the full time aperture T. Since such interval can be quite long (i.e., tens of seconds), a multistage approach is chosen comprising a coherent integration inside shorter intervals of duration T_f (here named frame and therefore representing the CPI) and a noncoherent integration among the N_f ($N_f = T/T_f$) frames. The overall processing comprises the following main stages.

1) Signal synchronization that tracks the parameters of the exploited direct signal to allow the regeneration of a noise-free replica of the reference signal to be used for range compression [27].
2) Range matched filtering that compresses the surveillance signal [28]. Despite the received reference and surveillance signals are continuous in time, they are formatted according to an equivalent fast-time τ/slow time u scheme, accounting for a fictitious pulse repetition interval (PRI) that can be matched to the GNSS primary code length. The range-compressed data in the (τ, u) domain can be written as

$$s_{\text{rc}}(\tau, u) = R_{\text{rs}}[\tau - R(u)/c] \cdot \exp\{j[2\pi f_d(u)\tau + \varphi(u)]\}$$
$$(10)$$

TABLE II
Analysis of Constraints on the CPI

target distance		200 m		500 m		1000 m		2000 m	
target velocity		T_{lin}	T_{quad}	T_{lin}	T_{quad}	T_{lin}	T_{quad}	T_{lin}	T_{quad}
5 kn	$\theta = 0°$	2.75	29.38	4.3	58.41	5.95	98.24	8.09	>100
	$\theta = 45°$	3.87	11.92	6	21.93	8.23	34.9	10.96	55.52
	$\theta = 90°$	61.9	>100	60.73	>100	58.94	>100	55.8	>100
10 kn	$\theta = 0°$	1.38	14.69	2.17	29.21	3.04	49.12	4.21	82.61
	$\theta = 45°$	1.95	5.961	3.05	10.98	4.24	17.43	5.82	27.69
	$\theta = 90°$	43.96	>100	43.54	>100	42.86	>100	41.6	>100
20 kn	$\theta = 0°$	0.7	7.3	1.09	14.06	1.54	24.56	2.15	41.3
	$\theta = 45°$	0.98	2.98	1.54	5.5	2.16	8.72	3	13.84
	$\theta = 90°$	31.06	>100	30.91	>100	30.67	>100	30.2	>100

where $\tau \in [0, \text{PRI}]$ and $u \in [-T/2, T/2]$, $R_{rs}(\cdot)$ is the cross-correlation function between the reference and surveillance signal and $R(u)/c$, $f_d(u)$, and $\varphi(u)$ are the instantaneous difference between direct and reflected signals in terms of delay, Doppler, and phase. A comment is in order concerning the mixed phase term $2\pi f_d(u)\tau$: being the reference and surveillance signals continuous in time, the aforementioned term accounts for the motion of the target during the single PRI. However, this term can be neglected considering the low values of typical Doppler frequencies of maritime targets and involved PRI.

3) Long time integration, which receives as input the range-compressed data and provides in output an integrated map related to the entire dwell time T where the target can be likely detected thanks to the recovery of suitable signal energy. The integration stage includes two main steps.

   a) Compensated maps formation: This step receives as input the range compressed signal and provides as output the sequence of the N_f maps after target motion compensation (TMC). Each compensated map coherently integrates the contributions from the target over an interval equal to T_f after correcting for target migration occurring inside the frame due to target motion. Moreover, interframes migration is also compensated in this step so that the same target is located in the same position in the sequence of the N_f maps. TMC can be performed in the local (X,Y) plane or in the basic Range & Doppler (RD) plane, providing the compensated maps $M_{m,\Xi}^{TMC}$ $m = -N_f/2, \ldots, N_f/2 - 1$, where $\Xi = XY$ or RD. The two options lead to different schemes and, therefore, are separately detailed in the following.

   b) Compensated maps integration: Thanks to the previous step, the target is located in the same position in all the compensated maps so that its returns can be properly noncoherently integrated, thus obtaining

the final integrated map, i.e.,

$$M_{\Xi}^{INT} = \frac{1}{N_f} \sum_m \left| M_{\Xi}^{TMC} \right|^2 \qquad (11)$$

where $\Xi = XY$ or RD depending on the specific choice to work with the local or basic plane technique, respectively. Thanks to the integration processing gain, the moving target can likely compete with the disturbance contributions, and therefore, be detected, for example, by applying a two-dimensional (2-D) CA-CFAR (cell averaging constant false alarm rate) scheme.

A. Local Plane Based Technique

In the local plane based technique, the formation of the generic compensated map is obtained by cascading two steps.

1) Sequence of RD maps formation—The entire dwell time T is segmented in consecutive batches of duration T_b such that constant reflectivity and negligible range and Doppler migration can be assumed. It has to be pointed out that the batch duration T_b is shorter than the frame duration T_f previously introduced: indeed the first defines the temporal unit for coherent integration without TMC, while the second corresponds to the basic CPI where TMC is carried out, as explained in the following point b). According to the results in Section II, the batch interval T_b can be reliably set equal to about 1 s. The nth batch is written as

$$s_{rc}^n (\tau, u) = s_{rc} (\tau, u) \cdot \text{rect}_{T_b} (u - u_n) \qquad (12)$$

where $u_n = nT_b + \frac{T_b}{2} n = -N_b/2, \ldots, N_b/2 - 1$ and $\text{rect}_{T_b}(u - u_n) = 1$ if $|u - u_n| \leq T_b/2$. Each batch is Fourier transformed with respect to the slow-time, thus obtaining a sequence of N_b range–Doppler maps $M_{RD,n}$ $n = -N_b/2, \ldots, N_b/2 - 1$ ($N_b = T/T_b$ here assumed even without loss of generality).
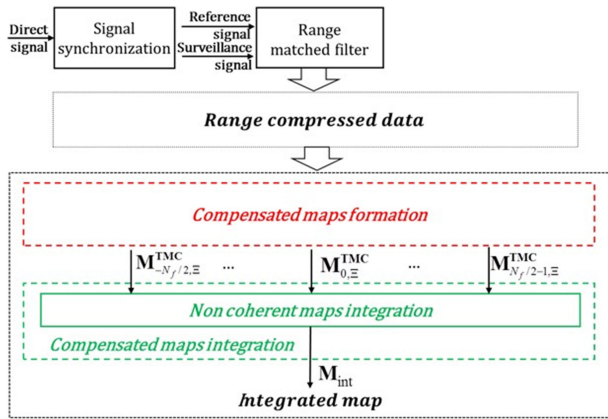
Fig. 4. Overall processing chain.

Fig. 5. Local plane target motion compensated map formation technique.

2) TMC—The range and Doppler position over, which the target is located at the nth batch depends on the batch time u_n, on target position at the reference time $\mathbf{p}^0_{TgT}$ and its kinematic parameters Θ_{TGT}, generally accounting for target velocity, acceleration, and higher order terms. This implies that target range and Doppler location changes with the considered batch due to target motion: namely, the target trajectory corresponds to a range and Doppler history that has to be tracked along the RD maps, with the ultimate goal to integrate the signal returns over the entire dwell time. Since target dynamics and position are unknown, all the possible combination of motion parameters Θ and location in the XY plane $\mathbf{p} = (x, y)$ must be considered. Therefore, to obtain the compensated map in the local plane, hereinafter indicated by $\mathbf{M}^{\mathrm{TMC}}_{m,XY}$, the proposed technique:

a) evaluates the corresponding range and Doppler histories $R(u_n, x, y; \Theta)$ and $f_d(u_n, x, y; \Theta)$ with $n = -N_b/2, \ldots, N_b/2 - 1$;

b) computes the mth compansated map coherently integrating the contributions from $N_{b/f}$ batches ($N_{b/f} = T_f/T_b$) according to

$$\mathbf{M}^{\mathrm{TMC}}_{m,XY}(x, y; \Theta) = \sum_{n=(m-1)(N_{b/f}-1)}^{n=m(N_{b/f}-1)} M_{\mathrm{RD},n}$$
$$\times [R(u_n, x, y; \Theta), f_d(u_n, x, y; \Theta)]e^{j\frac{2\pi}{\lambda}R(u_n,x,y;\Theta)}. \tag{13}$$

Following the previous description, the scheme in Fig. 4 is updated as in Fig. 5, where the "compensated maps formation" block is detailed as the cascade of the "RD maps formation" and "TMC" blocks.

The specific choice to work in the local plane, instead of directly in the basic plane (which is the common choice for conventional passive bistatic radar (PBR) systems used for detection purposes), offers some potential advantages: 1) such plane acts as a common reference when multiple transmitters are exploited, thus making the considered approach directly applicable to the multitransmitter case; 2) no simplifying range or Doppler polynomial models have been considere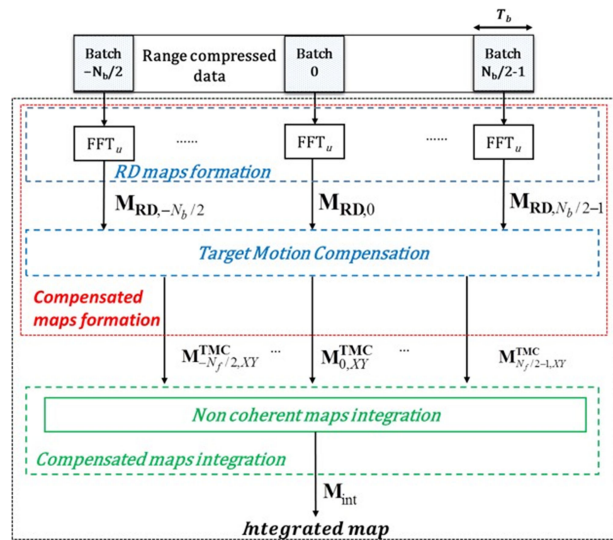d so far, therefore, for each assumed motion condition, the exact track of the range and Doppler histories allows a complete compensation of the migration, and therefore, the highest integration gain. As drawbacks: 1) the tracking and, thus, the integration needs to be separately evaluated for each position $\mathbf{p}(x, y)$ and motion Θ of the candidate target, thus generally increasing the computational load; 2) the compensated maps will show a spatially variant correlation arising from the projection from the basic to the local plane as it will be shown in Section IV. Finally, it is worth to explicitly mention that the proposed technique can also be suitable for a double application comprising both short time (for big and/or close targets) and long time (for small and/or far targets) integration techniques: in fact the sequence of range–Doppler maps obtained in the first step could be suitably exploited for this purpose as commonly done in conventional PBR systems.

B. Basic Plane Based M-MTI

The previous technique exploits the actual range and Doppler variation as a function of the supposed motion parameters, without any approximation. Consequently, the process of TMC appears to be computationally demanding. A more efficient procedure can be obtained in the basic plane under the assumption that a linear approximation of the Doppler history suffices, according to an unknown slope represented by the Doppler rate. Based on the analysis in Section II, this assumption is reasonable for integration times of some tens up to one hundred of seconds. Differently from the local plane based technique, TMC does not compensate for the actual target trajectory, but it accounts for Doppler and range migration correction according to the considered polynomial model. In this case, TMC works directly on the data strip obtained by selecting the proper slow-time interval of duration T_f

$$s^m_{\mathrm{rc}}(\tau, u) = s_{\mathrm{rc}}(\tau, u) \cdot \mathrm{rect}_{T_f}(u - u_m). \tag{14}$$
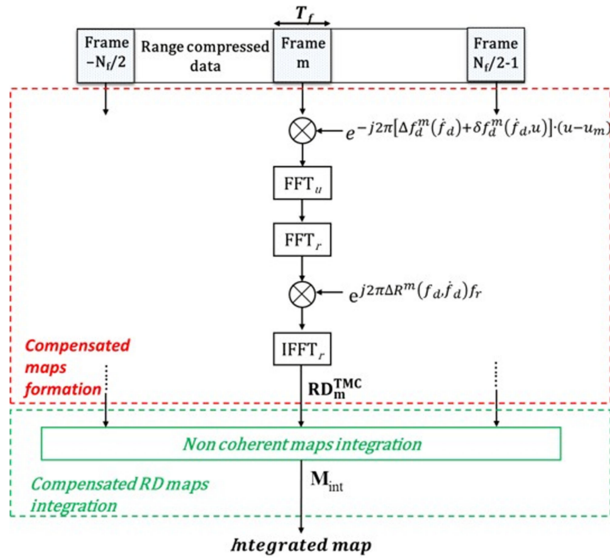
Fig. 6. Basic plane target motion compensated map formation technique.

In this case, Doppler migration can occur both inside the single frame and through the frames. Specifically, Doppler migration inside the frame is described by the law

$$\delta f_d^m(\dot{f}_d, u) = \dot{f}_d \cdot (u - u_m) \cdot \mathrm{rect}_{T_f}(u - u_m) \quad (15)$$

while the Doppler migration from the mth frame to the reference one ($m = 0$) can be written as

$$\Delta f_d^m(\dot{f}_d) = f_d^m - f_d^0 = \dot{f}_d m T_f, \quad (16)$$

$\dot{f}_d$ being the Doppler rate of the target corresponding to motion condition of interest Θ. Due to the coarse range resolution, range migration is assumed occurring only among the frames and (after compensation of Doppler migration) described by

$$\Delta R^m\left(f_d, \dot{f}_d\right) = R^m - R^0 = -\lambda \left[f_d m T_f + \dot{f}_d \frac{(m T_f)^2}{2} \right]. \quad (17)$$

Therefore, Doppler migration is corrected in the (range R, slow-time u) domain by multiplying by a phase term comprising both sources of migration in (15) and (16), whereas range migration is compensated by multiplying the mth map in the (range frequency f_r, Doppler frequency f_d) domain for a phase term according to (17). Following the previous description, the scheme in Fig. 4 is updated as in Fig. 6. This provides a set of N_f range Doppler compensated maps ($\boldsymbol{M}_{m,\mathrm{RD}}^{\mathrm{TMC}}$) where targets moving according to the condition under test have been correctly aligned to their range–Doppler position occupied at the reference time instant.

This scheme properly generalizes the one presented in [26] and [27] because of the following reasons.

1) It allows the consideration of higher CPIs requiring a compensation not only of the Doppler variation among the different data segments noncoherently integrated [interframes migration, (16)] but also of the Doppler spread

occurring inside the single frame [intraframe migration, (15)] that cannot be negligible as proved by results in Table II.

2) It reduces the computational load by switching the order of range and Doppler migration compensation and by nicely merging the Doppler migration compensation with the RD map formation step, thus saving two fast Fourier transforms (FFTs) with respect to slow-time domain.

C. Filters Bank Design Criteria

As it has been already underlined, it should be pointed out that the procedure described above depends on the unknown target motion parameters. In particular, the local plane based technique will provide in output a set of $\boldsymbol{M}_{XY}^{\mathrm{INT}}(x, y; \Theta)$ maps, one for each tested motion parameter vector Θ; the basic plane based technique instead will provide in output a set of $\boldsymbol{M}_{\mathrm{RD}}^{\mathrm{INT}}(r, f_d; \dot{f}_d)$, one for each tested Doppler rate. Therefore, a completely adaptive technique is obtained by resorting to a filter bank performing the formation of the compensated maps according to specific sets of values. Suitable criteria for the design of such bank for both local and basic plane are provided in this section. Particularly, for sake of simplicity, we will refer to a target moving at almost constant speed, that is $\Theta \equiv v = (v_x, v_y)$: this simplifying hypothesis appears reasonable for not maneuvering targets such as ships sailing at cruising speed. Nevertheless, the proposed approach could be easily generalized to cope with different situations.

As far as the local plane based technique is concerned, the required sampling on the (X, Y) plane and the grids of tested velocities need to be defined. The bounds on (X, Y) plane are defined according to the surveilled area, while the ones on v_x and v_y are set according to the maximum possible target speed.

The sampling step on (X, Y), denoted as δx and δy, respectively, should be at least equal to the best range and azimuth resolutions provided by the system. Since the best resolution values are obtained for the pseudomonostatic geometry, they can be set equal to

$$\delta x \leq \alpha_r \frac{c}{B} \ \& \ \delta y \leq \alpha_d \frac{\lambda R_{\min}}{T_f \left| v_{y\,\max} \right|} \quad (18)$$

where $R_{\min}$ is the minimum considered range and $\left| v_{y\,\max} \right|$ the maximum target tangential speed; α_r and α_d are the range and azimuth resolution shape factors.

The sampling of the (v_x, v_y) plane can be derived assuming v_x mainly responsible for range migration and v_y responsible for Doppler migration. The sampling step of v_x has to assure a residual range variation between the reference and the last frame less than half range resolution cell. Letting δv_x be the uniform step size of v_x, this has to fulfill

$$\delta v_x \leq \alpha_r \frac{c}{N_f T_f B}. \quad (19)$$

The sampling of v_y has to assure a residual Doppler variation from the reference to the last frame less than half Doppler resolution cell (being the Doppler resolution equal

TABLE III
Satellite and Processing Parameters

Parameter		Value	unit
Satellite	Satellite number	GSAT0103	-
	Ranging code	PRN19 (E5a-Q primary code)	-
	Satellite azimuth (relevant to North)	61.6~62.1	deg
	Satellite elevation (relevant to receiver)	70.7~70.8	deg
	Power density at ground level	-135	dBW/m^2
Processing parameters	Sampling frequency	50	MHz
	Equivalent pulse repetition interval	1	ms
	Central frequency	1176.450	MHz
	Operating bandwidth	10.230	MHz
	Dwell time	30	s

to $1/T_f$). Considering a target at range R, moving at v_y and compensated according to $v_y + \delta v_y$, this leads to an uncompensated Doppler rate equal to $(2v_y \cdot \delta v_y + \delta v_y^2)/(\lambda R)$: thus, the above-mentioned requirement imposes the following constraint:

$$\frac{2v_y \cdot \delta v_y + \delta v_y^2}{\lambda R} \cdot \frac{N_f T_f}{2} \leq \frac{1}{2T_f}$$

$$\xrightarrow{\text{yields}} \begin{array}{ll} \delta v_y \leq -v_y + \sqrt{v_y + \lambda R_{\min}/(N_f T_f^2)} & v_y \geq 0 \\ \delta v_y \leq -v_y - \sqrt{v_y + \lambda R_{\min}/(N_f T_f^2)} & v_y \leq 0 \end{array}.$$

(20)

Therefore, (20) can be used for the design of the bank resulting in a not uniform sampling of the v_y axis.

Moving to the basic plane technique, only the criterion for the sampling of the Doppler rate axis needs to be defined. Particularly, the bounds on the spanned interval $[-\dot{f}_{d\max}, +\dot{f}_{d\max}]$ can be set according to the maximum considered Doppler rate (for example, corresponding to a target at the minimum distance moving at the highest tangential speed); the sampling step over this interval has to assure a residual Doppler variation between the center and the extreme of the dwell time below $1/(2T_f)$: this results in a constraint given by

$$\delta \dot{f}_d \leq \frac{1}{N_f T_f^2}$$

(21)

providing a uniform sampling.

IV. THEORETICAL PERFORMANCE ANALYSIS

The effectiveness of the proposed detection techniques is tested and demonstrated in this section against synthetic data: main satellite and processing parameters are listed in Table III while receiver parameters are as in Table I. A satellite of the Galileo constellation has been considered as transmitter of opportunity, whose estimated trajectory was obtained from a GNSS satellite tracking website [36]. We considered a ship navigating in the field of view of the surveillance antenna, with position $\boldsymbol{p}_{\text{TgT}}^0 = (122\,\text{m}, 100\,\text{m})$ at the reference time, moving at a velocity of 10 kn with heading 45° with respect to the $x-$ direction, corresponding to a bistatic range and Doppler position equal to 1493 m and -16.33 Hz. The target RCS has been set equal to 100 m^2. Concerning the disturbance background, we assumed a white Gaussian noise according to parameters in Table I. Therefore, not any strategy for suppression of sea clutter has been taken into account here. This follows from the assumption that the system is mainly noise-limited rather than clutter-limited, as a consequence of the restricted power budget provided by GNSS and the long dwells considered, acting as a whitening filter with respect to the background distribution. It could be shown that such a hypothesis is well in line with the experimental datasets collected during the field trials whose results are presented in the next section. In addition, possible interfering e.m. sources have been neglected taking into account that the signals that do not match with the pseudo random noise (PRN) code of the useful signal will be discarded during the matched filtering and the proposed long integration time techniques are expected to spread possible interference over multiple resolution cells.

First, let us consider a conventional approach to detect the moving target consisting in looking for the peak in the RD map obtained over a short CPI. After the range-compression has been performed, we could select a time interval around the reference time of the acquisition short enough to ensure that the target reflectivity is constant and migration negligible. By means of a slow-time FFT, we achieved the corresponding RD map. As examples, Fig. 7 shows the obtained results for intervals durations equal to 1 and 3 s. In the figures, 0 dB represents the mean noise background power level and the black star markers denote the target range and Doppler actual location. As it is apparent, it is not possible to individuate any bright spot that can be associated to the target. Namely, the coherent integration gain achieved over limited time windows did not suffice to detect the target. The results obtained by using the proposed long integration time techniques are provided in the remainder of the section.

A. Local Plane Based Technique Results

The local plane based technique requires the definition of the batch duration T_b and the number of batches $N_{b/f}$ to be coherently combined to form a frame. Here, we set $T_b = 1$ s while for the $N_{b/f}$ we adopted two choices: in the former, $N_{b/f} = 1$, which means that $T_f = T_b = 1$ s and $N_f = 30$ frames are noncoherently integrated; in the latter, $N_{b/f} = 3$, namely $T_f = 3$ s and $N_f = 10$ frames are noncoherently integrated. The searching grids over the space and velocity domains are set according to the criteria in Section III-C, thus obtaining two different sets of $\boldsymbol{M}_{XY}^{\text{INT}}(x, y; \boldsymbol{v})$ maps for the two different CPI options.

Let us consider first the case in which $\boldsymbol{v} = \boldsymbol{v}_{TgT}$. Fig. 8 shows the resulting $\boldsymbol{M}_{XY}^{\text{INT}}$ maps, where Fig. 8(a) and (b) refer to the case of $T_f = 1$ s and $T_f = 3$ s, respectively.
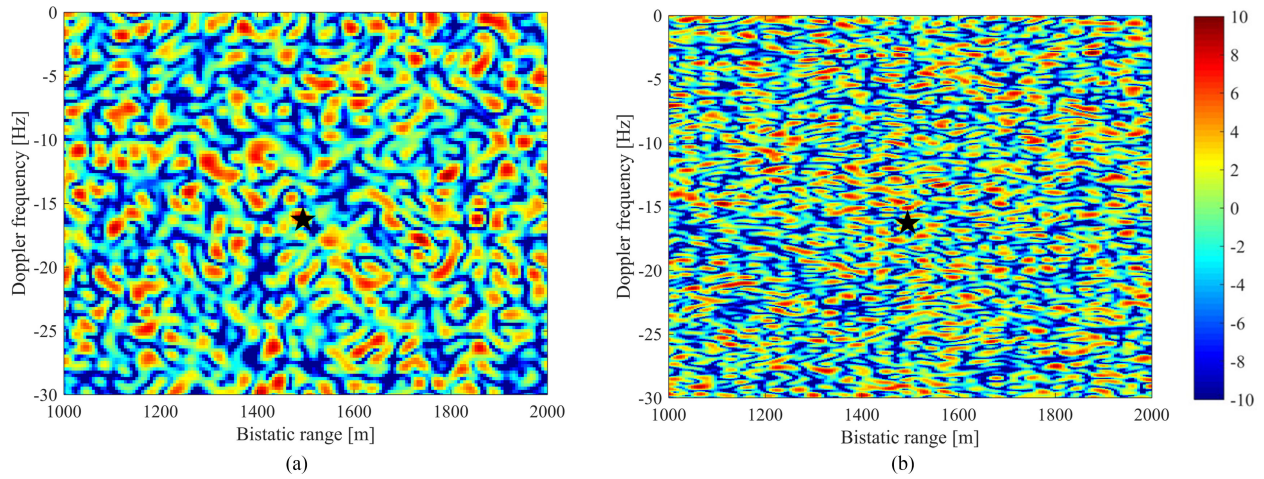
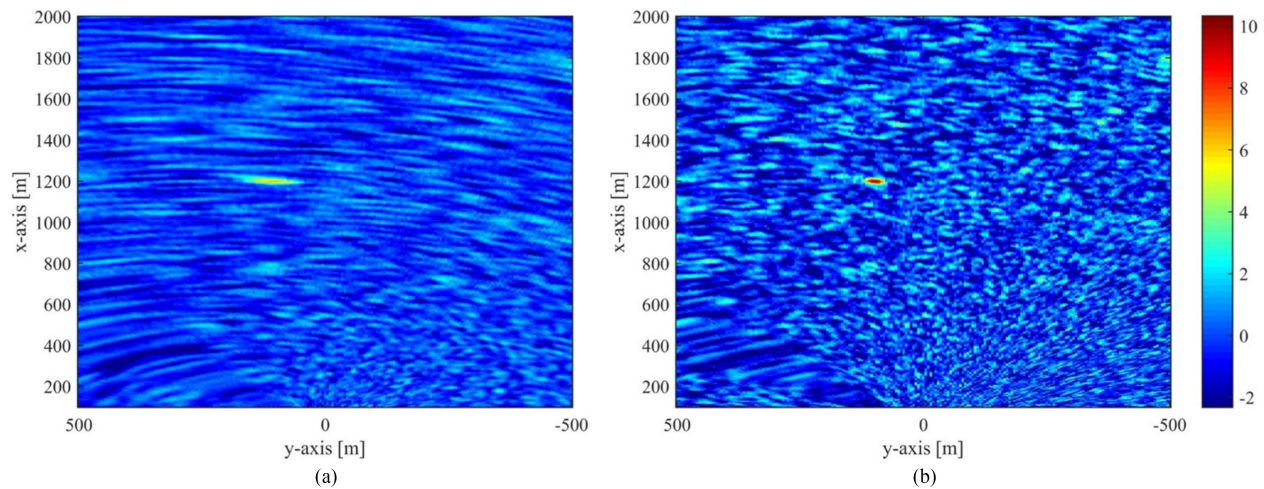Fig. 7. RD maps obtained over individual CPIs. (a) CPI = 1 s. (b) CPI = 3 s.

Fig. 8. Integrated local map for the actual target velocity. (a) $T_f = 1$ s. (b) $T_f = 3$ s.

It should be pointed out that the mean power of the background is the same of the single RD maps in Fig. 7 obtained over the same CPI, whereas their standard deviation reduces by approximately $\sqrt{N_f} = 5.48$ and 3.16 times in Fig. 8(a) and (b), respectively, according to the number on noncoherently integrated maps. At the same time, the target motion is correctly compensated in the integrated maps pertaining the actual target velocity; thus, the target energy is correctly accumulated over the entire dwell. Indeed, in both the figures a bright spot can be observed in the position corresponding to the actual target location. Comparing the two figures, we can observe the higher intensity and the better resolution in Fig. 8(b), because of the longer CPI. Moreover, from both figures, it can be easily noticed the particular appearance of the background due to the spatially variant correlation characteristics induced by the projection into the local plane. This can be easily understood by recalling the spatially variant behavior of the point spread function evaluated on the local plane [16]. As mentioned in Section III-A, the local plane based technique entails a spatial correlation in the local plane, due to the spatially variant

shape of the range and Doppler resolution cell projected onto the ground plane.

Fig. 9 shows the cuts around the peak position along the x and y directions. The blue dotted line refers to the map obtained without the TMC procedure (in the case of $T_f = 1$ s), which would correspond to the map obtained for the tested null velocity; the red and green curves refer instead to the maps in Fig. 8(a) and (b), respectively. As it is apparent, the TMC is a mandatory step to effectively integrate the signal energy during the long dwell. Indeed, the blue curve does not show any clear peak, because the target energy has not been correctly gathered during the dwell time. In contrast, the correct tracking of the range and Doppler history enabled by the TMC procedure allows building up the target energy resulting in clear peaks for the red and green curves. We can observe the higher peak intensity reached with the longer CPI, whereas the background fluctuations are lower in the shorter CPI case because of the greater number of noncoherently integrated maps. Since at short/medium range from the RX the differential bistatic range is almost equal to the range from the
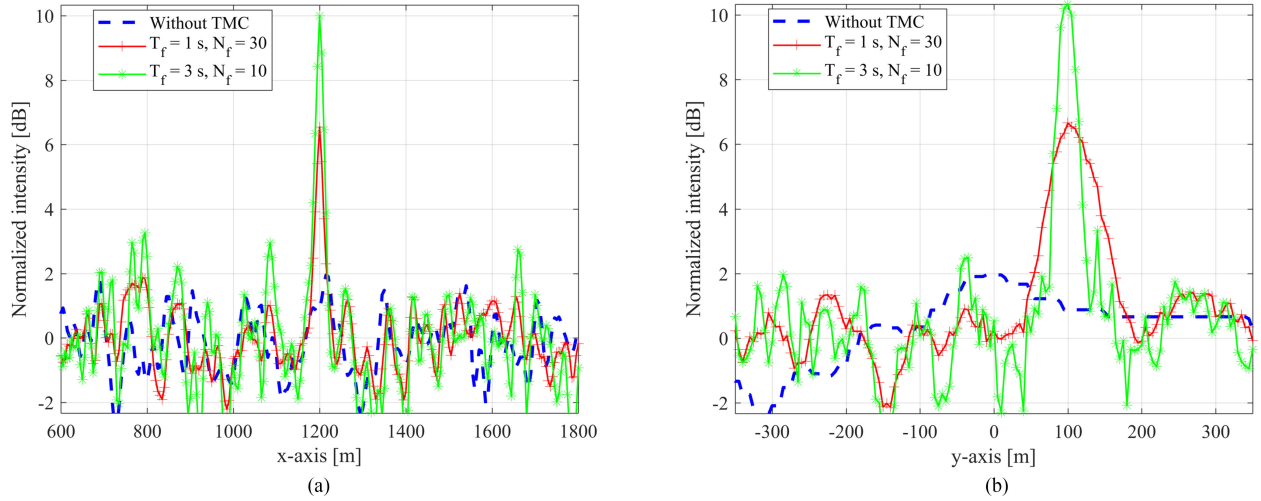
Fig. 9.   Cross-sections around the actual target position. (a) *x*-axis cross section. (b) *y*-axis cross section.

receiver here represented by *x*-direction and for the considered geometry (distance TX–TgT>>distance TgT–RX) and limited CPI the receiver only contributes to the target Doppler bandwidth causing a cross-range direction almost coinciding with *y*-direction, when increasing the CPI (i.e., moving from $T_f = 1$ s to $T_f = 3$ s) the resolution remains unchanged along the *x*-axis [see Fig. 9(a)] whereas it increases along the *y*-axis [see Fig. 9(b)].

Obviously, since the target speed is generally unknown, all the maps corresponding to the tested velocities have to be screened. In this respect, we have to note that there is an inherent ambiguity in the local plane based technique, lying in the fact that different combinations of positions and velocity may give rise to approximately the same range and Doppler history. Therefore, as well as the detection of the target in the correct position and the estimation of its actual velocity, the local plane based MTD technique might provide detections in false positions associated at wrong estimated velocities. We anticipate here that also the basic plane based technique suffers for an ambiguity problem. Therefore, the discussion concerning this issue is postponed to Section IV-C where the performance of the two approaches is compared.

B. Basic Plane Based Technique Results

In this section, we present the results obtained with the basic plane based integration technique along the line of what has been presented for the local plane based technique. For each value of Doppler rate under test, the $M_{RD}^{INT}(R, f_d; \dot{f}_d)$ map is obtained according to the selected frame duration. As for the local plane based technique, the two cases $T_f = 1$ s and $T_f = 3$ s have been considered. Fig. 10 shows the integrated RD maps when the TMC has been accomplished using the actual target Doppler rate (equal to 0.0395 Hz/s). We can observe that also the suboptimum technique allowed retrieving a suitable signal to disturbance power ratio to isolate the target from the background. These maps can be compared with the short time

RD maps shown in Fig. 7: the integration of multiple RD maps, along with the TMC according to the actual Doppler rate, can enable the detection of the target otherwise inhibited in the single RD maps. Fig. 11 shows the range and Doppler cuts around the peak position, along with the curve resulting from the integration performed skipping the TMC procedure (blue dotted line). We can observe that also for this technique the TMC represents a mandatory step to correctly concentrate the target energy during long dwells. In addition, as before, higher SNR and better Doppler resolution are achieved considering longer CPIs.

While the unknown target motion makes necessary for the local plane based technique to screen all the M_{XY}^{INT} maps pertaining different velocities, for the basic plane based case it makes it necessary to screen all the M_{RD}^{INT} maps pertaining different Doppler rates. Despite values of the Doppler rates different from the actual one result in a perturbed TMC, depending on the particular conditions, detections could occur in more M_{RD}^{INT} maps pertaining different Doppler rates. As for the local plane based technique, the discussion about this issue is postponed to Section IV-C.

C. Performance Comparisons

Previous results showed how both techniques can collect the target energy over long integration times, thus enabling its detection. In this section, we compare the two techniques in terms of achievable performance, in order to outline their pros and cons in real-word applications.

First, it should be pointed out that the local plane based technique can exactly track the range and Doppler history of the target (provided the correctness of the assumed motion model), and therefore, in principle, it is able to accurately integrate the target contributions, thus yielding the highest gain. In contrast, the basic plane based technique assumes a linear migration of the target in the Doppler domain that, depending on the particular conditions, could be not sufficiently accurate (see also Section II). Therefore, with the increase of the integration time, the basic
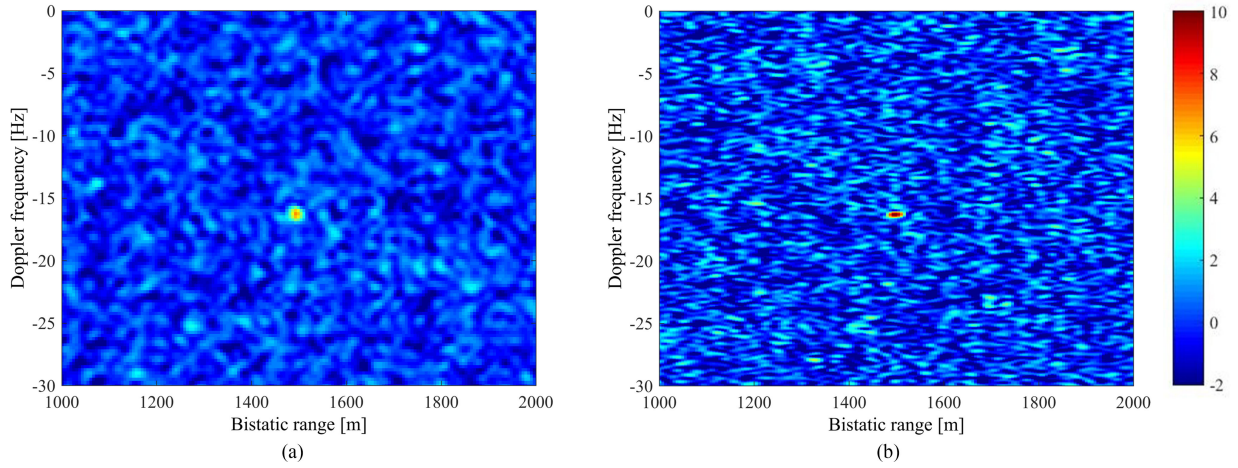
Fig. 10. Integrated RD map for the actual Doppler rate. (a) $T_f = 1$ s. (b) $T_f = 3$ s.
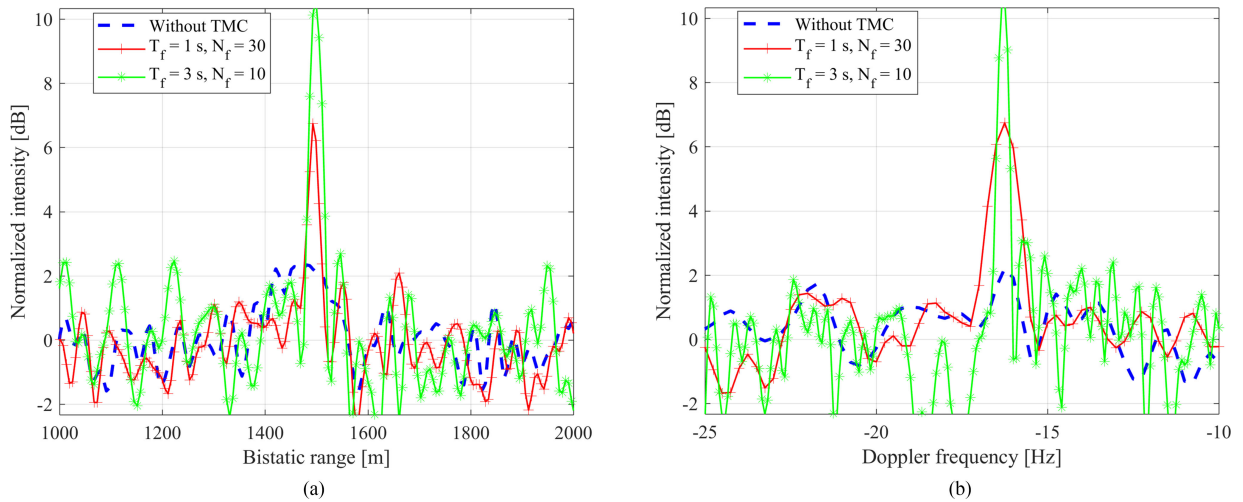

Fig. 11. Cross-sections around the actual target position. (a) Bistatic range cross section. (b) Doppler cross section.

plane based technique may experience some performance degradation, because of the mismatch between target phase history and the assumed model. To analyze the degradation in integration gain of the basic plane based technique, we evaluate the maximum dwell time for which such technique loses a maximum of 3 dB with respect to the optimum integration, reached by the local plane based technique, for different target distances and velocities. Moreover, in order to quantify the improvement due to the compensation of both intraframe and interframe migration with respect to interframe migration only, results obtained by neglecting intraframe migration (as done in [26], [27]) are also analyzed. It is worth to note that for the purpose all the calculations do not take into account the length of time a target may be in the field of view of the surveillance antenna. The obtained results are reported in Table IV: for each velocity and range couple the first reported value (blue font) refers to the case of intra- and interframe migration compensation while the second one (red font) concerns interframe only. From the table, we observe that in most cases the dwell time should be increased over 100 s to appreciate

TABLE IV
Analysis of the Losses of the Basic Plane Based MTD Technique:
Maximum Time Dwell for Losses Lower than 3 dB

Target distance / Target velocity ($\theta = 45°$)	200 m	500 m	1000 m	2000 m
5 kn	61 s	> 100 s	> 100 s	> 100 s
	60 s	> 100 s	> 100 s	> 100 s
10 kn	22 s	55 s	>100 s	> 100 s
	18 s	53 s	>100 s	> 100 s
20 kn	8 s	20 s	39 s	80 s
	< 3 s	<3 s	35 s	77 s
30 kn	7 s	12 s	23 s	44 s
	< 3 s	< 3 s	< 3 s	38 s

significant losses: this implies that in many practical applications the two techniques are equivalent in terms of integration gain. The main losses are observed for those
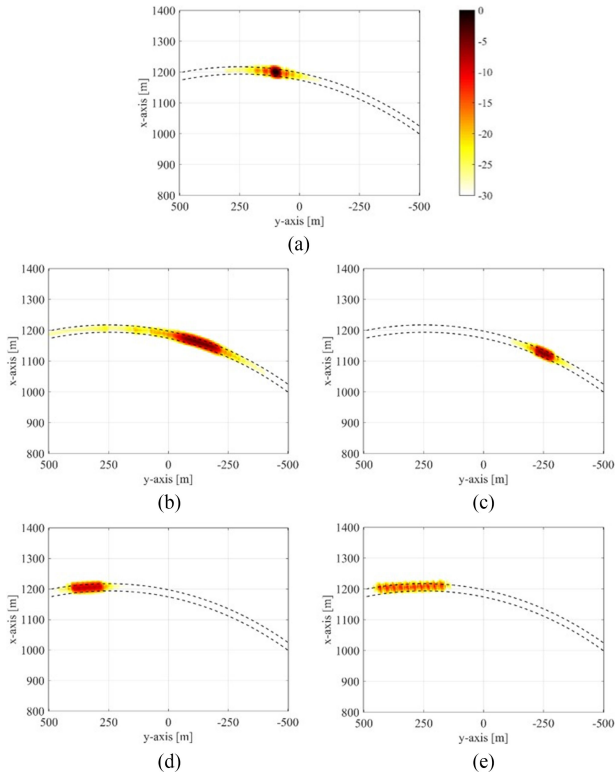
Fig. 12. Local plane maps for different values of the tested velocity.
(a) $v_x = v_y = 3.64$ m/s (actual speed). (b) $v_x = 3.64$ m/s $v_y = 1.25$ m/s.
(c) $v_x = 4.61$ m/s $v_y = 3.64$ m/s. (d) $v_x = 3.64$ m/s $v_y = -5.34$ m/s. (e)
$v_x = 3.64$ m/s $v_y = -10.02$ m/s.

Fig. 13. Basic plane maps for different values of the tested Doppler
rate. (a) $\dot{f}_d = \dot{f}_{d\mathrm{TgT}} = -0.0395$ Hz/s. (b) $\dot{f}_d = -1.3000$ Hz/s.
(c) $\dot{f}_d = -0.6778$ Hz/s. (d) $\dot{f}_d = 0.2889$ Hz/s. (e) $\dot{f}_d = 1.3000$ Hz/s.

targets moving at high speed and at near ranges. Indeed, a target moving with high velocity and at close range exhibits a Doppler history that cannot be assumed as linear, thus 1) making mandatory the compensation of the intraframe migration as visible from the results reported in red in the table; 2) entailing a lower capability of the technique to follow the range and Doppler history over long dwells as visible from the results reported in blue in the table. Nevertheless, it is worth to point out that targets at closer ranges generally require shorter integration times to become detectable, thus partially overcoming point 2).

As mentioned earlier, the unknown target kinematic makes necessary to inspect all the M_{XY}^{INT} or $M_{\mathrm{RD}}^{\mathrm{INT}}$ maps pertaining the different tested conditions. To show clearly the effect of TMC accomplished according to different velocity/Doppler rate values, an analysis in noise-free background is now provided.

Fig. 12 shows five M_{XY}^{INT} maps achieved for different tested velocities; in the maps, 0 dB represents the higher intensity value that has been obtained among all the maps and it corresponds, as expected, to the map pertaining the actual target velocity [see Fig. 12(a)]. In the remaining maps, we can observe that the technique provided a lower integration gain, spreading the target energy over larger areas. Nevertheless, depending on the specific conditions (i.e., input signal to disturbance ratio), more maps could result in undesired detections, which could be referred to as ghosts. However, the positions of such ghosts are not
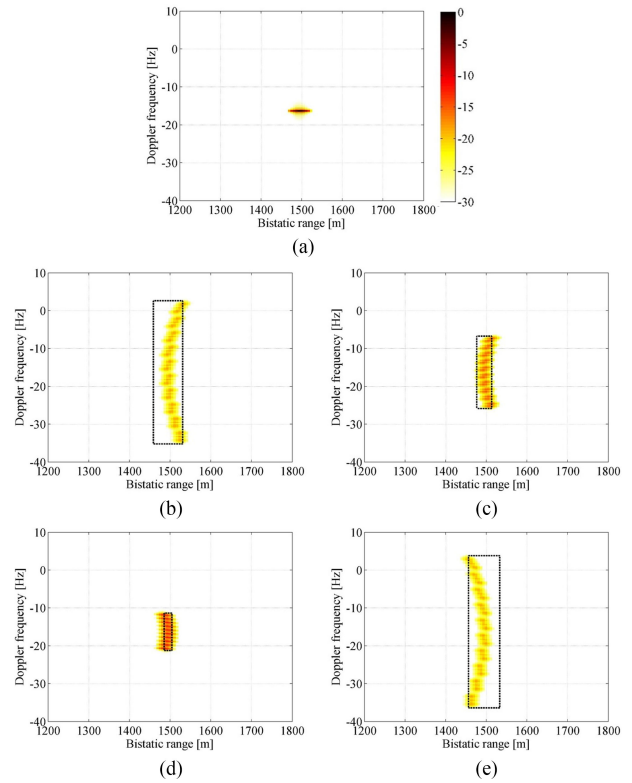
fortuitous. The black dotted lines in the figures represent the bistatic isoranges at $R(0) \pm \frac{c}{2B}$. As it is apparent, all the ghosts locate on an isorange area. It is easy to understand that for an individual target the application of a decision threshold to each M_{XY}^{INT} map could result in a number of detections filling an isorange area, whose width is related to the chip rate of the transmitted signal. Therefore, the local plane based technique is able to provide a good accuracy in range, whereas its angular accuracy is likely limited by the beamwidth of the surveillance antenna. However, it is worth noting that the orientation of the bistatic isoranges depends on the particular bistatic geometry. As mentioned previously, one of the bigger benefits of GNSS is the multitude of satellites simultaneously illuminating an area. The multiple bistatic links arising from the exploitation of multiple satellites give rise to different location of the ambiguities, thus enabling their rejection by means of multilateration.

Fig. 13 shows $M_{\mathrm{RD}}^{\mathrm{INT}}$ maps obtained for five different values of the Doppler rate. As for the previous analysis, these maps have been obtained in noise-free conditions and 0 dB represents the highest intensity value, which has been obtained for the map pertaining the actual Doppler rate reported in Fig. 13(a). The accomplishment of the TMC procedure driven by a wrong value of the Doppler rate entails that Doppler migration inside the frame is not correctly compensated, from (15), and Doppler and range migration from the mth to the reference frame are not correctly corrected, from (16) and (17). The former effect entails a

blurring effect at the single compensated map formation level, whereas the latter results in different positions of the target in the $M_{m,\text{RD}}^{\text{TMC}}$ maps so that in the final integrated map a further blurring effect can be observed [see Fig. 13(b)–(e)], with the energy spread over multiple cells. The black dotted rectangle in the figure highlights the area of the basic plane where the target energy can be spread. This can be obtained by evaluating the maximum co-registration errors in range and Doppler position obtained at the border of the processed dwell time and respectively equal to $\frac{|\dot{f}_d - \dot{f}_{d\text{TgT}}|T^2\lambda}{8}$ and $|\dot{f}_d - \dot{f}_{d\text{TgT}}|T/2$ being in this case $\dot{f}_{d\text{TgT}}$ the actual target Doppler rate and $\dot{f}_d$ the generic value used by the technique. Compared to the local plane case, as visible from Figs. 12 and Figs. 13, the ghosts generated in the basic plane locate on the actual target position. The above characteristic, combined with the deterministic shape of the ghost, could be exploited by a proper post detection logic for ghost removal.

It is worth to point out that, because of the occurrence of these ambiguity regions, a strong target might mask a weaker one. For the local plane based technique, this may be the case if two targets are on the same isorange area, whereas for the basic plane based approach, if the RD position of the weaker target is inside the area of the basic plane over which the stronger target energy is spread. However, it should be noted that such an issue could be solved by considering successive integration windows or even better exploiting multiple bistatic links in the scenario involving multiple satellites.

Furthermore, we pointed out that so far both techniques were derived and tested considering a target undergoing translation motion only. Actually, we do not expect more complex kinematics to prevent the detection capability provided by the presented long integration time techniques. If a target experiences yaw, pitch, and roll along with translational motion, target will slightly spread in the range–Doppler domain around the position occupied by target fulcrum (i.e., the center of rotation). However, considering the available range resolution and wavelength of GNSS waveforms, we expect the RD cluster of points pertaining to the target to be small, thus not preventing energy collection and consequent target detection. Indeed, it is worth noticing that the long integration concept and performance of the proposed techniques are expected to still hold since both techniques adaptively compensate the translation motion, thus aligning the clusters corresponding to different frames around the same position. Therefore, the aligned clusters can be noncoherently integrated, even in presence of such rotation motions, thus enabling target detection.

As a final remark, we observe that, considering the complementary characteristics of the two techniques, the local plane based approach can be suitable for the detection of targets following specific trajectories of interest *a priori* defined (so that the computational load is kept under control), while the basic plane technique appears as a good candidate for the surveillance of wide areas on a permanent basis and when near real time is required.
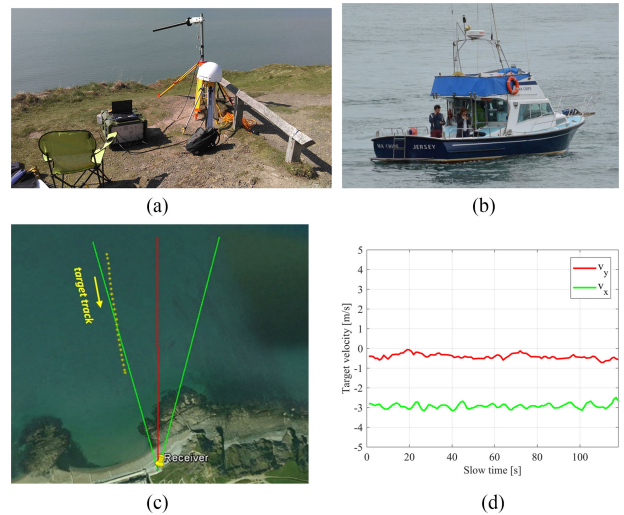

Fig. 14. First maritime experimental campaign. (a) Receiving hardware. (b) Cooperative target. (c) Acquisition geometry. (d) Recorded target speed.

V. EXPERIMENTAL RESULTS

To prove the effectiveness of the proposed algorithms, two proofs of concept measurement campaigns have been conducted by means of the experimental receiver developed at University of Birmingham and shown in Fig. 14(a). It should be stressed that the experimental receiver was scientific equipment, thus not specifically tailored for the type of application considered in this paper. For this purpose, experiments were done with the receiver on the shore, and targets of substantially varying dimensions were used. Therefore, the overall purpose of these experiments was to confirm the functionality of the proposed techniques and to quantify their relative performance, rather than investigating the absolute detection performance of a GNSS-based radar system, which is a separate topic.

The receiver itself was equipped with two RF channels for recording both the direct and surveillance signals, respectively. A low gain antenna was used to record data from all available satellites feeding the reference channel and representing the direct signal for the following bistatic processing; as GNSS signals are right-hand circularly polarized (RHCP), the reference antenna was RHCP. The surveillance channel acquired the weak radar signal through a high-gain antenna steered toward the surveilled area; to minimize the direct path interference, a left-hand circularly polarized antenna was used.

A. Experimental Campaign With Cooperative Target

The first experimental campaign was conducted near Aberystwyth (U.K.) [26]. GLONASS was selected as transmitter of opportunity and returns from a cooperative target acquired, as shown in Fig. 14(b). This target was a small fishing boat, approximately 10 m long. Such a vessel was used in the first instance because it was possible to rent and equip it with a GPS receiver, while following a desirable trajectory on a straight line from the sea and toward

TABLE V
Experimental and Signal Processing Parameters of the First Maritime
Acquisition Campaign

Parameter		Unit	Value
Satellite	number	-	732
	carrier frequency	MHz	1603.6875
	Chip rate	MHz	5.11
	azimuth (clockwise from N)	deg	3.0 ~ 6.8
	elevation (relevant to HC)	deg	73.2 ~ 73.1
Processing parameters	sampling frequency	MHz	50
	pulse repetition interval	ms	1
	dwell time	s	118
	frame duration	s	3
	non-coherent integrated frames	-	20

the shore. This allowed us to be aware of the acquisition scenario, which is depicted in Fig. 14(c). The target was approaching the receiver with a velocity of about 5 kn, persisting in the main lobe of the receiver antenna for most of the acquisition time. Fig. 14(d) shows the recorded target speed components.

Table V shows transmitter and processing parameters. In particular starting from an acquisition length of 118 s, T_f has been set to 3 s, while the noncoherent integration time has been set to 60 s. Indeed, in this case, we foresee the necessity of long integration times and TMC, differently from the case presented in [27], where the high RCS of the acquired ship allows it to be detectable even with short coherent integration time.

Fig. 15(a) shows the RD map achieved with a coherent integration of 3 s. From this figure, the presence of the direct signal well concentrated around the zero range and zero Doppler frequency position along with its sidelobes can be seen. Its cancelation along with the stationary background could be considered, [37], but here we retained it to compare it with the amplitude levels of clutter and target.

While a strong and well visible return is present around 50 m in range and spreading over several Doppler positions that can be related to clutter, the target return, whose actual GPS position is marked with the white "×" in the figure, is buried under the disturbance level and, therefore, not visible, as it is apparent from the enlargement around the true target position shown in the white box. The short CPI of 3 s does not guarantee an effective integration gain; therefore, a longer integration is mandatory. The RD map resulting from the direct noncoherent integration over a longer time, but without TMC, is shown in Fig. 15(b), purely for visualization purposes and to compare it to the case comprising TMC. Although the disturbance fluctuations have been reduced, it is not possible to see the target return, which is an expected result since over this time the target has moved over several resolution cells.

Results from the local plane based technique are shown in Fig. 16. Each image is obtained by performing a first coherent integration of 1 s batches, yielding to $N_b = 60$ RD maps, and then a second coherent integration step over 3 s frames yielding $N_f = 20$ motion compensated local maps that are finally noncoherent integrated. The three images are normalized to the mean disturbance level and each one corresponds to a different start time, 0 s, 30 s, and 58 s for Fig. 16(a)–(c), respectively. They show the output of the local plane based MTD technique corresponding to the tested target velocity vector $v_{T_gT} = [-2.9, -0.5]$ m/s providing the maximum SNR. In all the presented images, the target return is well visible above the disturbance level meaning that the implemented technique allowed recovering a better SNR value. Moreover, target returns are well in line with the expected position retrieved from GPS data, shown as with "×" markers in the images. In agreement with results in Section IV, a spatially variant correlation of the background is observed. Finally, the effect of a more favorable link budget is also evident as the considered start time increases: indeed the target was approaching the radar receiver; therefore, higher target power is expected as the integration window slides over the whole acquisition.

Results obtained in the RD domain are shown in Fig. 17; the same parameters of the local plane based technique have been used. Particularly, Fig. 17 shows the output of the basic plane based MTD technique corresponding to the Doppler rate value providing the maximum SNR. As it is apparent from the zooms in the white boxes of the area around the true target position, target return is well visible above the disturbance level, implying the recovery of an SNR level suitable for detection. Moreover, as already verified in the local plane based MTD technique performance analysis, it is clear from a visual inspection how this level increases as the start time increases.

As explained in Section II-A, and differently from the local plane based technique, the proposed procedure operates under the hypothesis that a second order approximation is sufficient to accurately describe the variation with time of the target distance from the radar. To verify that this hypothesis holds in the experimental study case, we performed the basic plane based MTD technique exploiting the *a priori* information available from the GPS records of the target. To this purpose, in the range and Doppler frequency coregistration steps, the TMC has been performed exploiting the actual differences between the target range and Doppler frequency at the current frame time with respect to the target range and Doppler frequency at the reference time instead of the quantities shown in Fig. 6. Fig. 18 shows the range and Doppler frequency cuts of the target response when *a priori* information on the target motion is used for the integration window starting at 58 s. From a visual inspection there is a good correspondence between the target response pertaining to the proposed technique (red curves) and the ones pertaining to the exploitation of the *a priori* information of the target motion (blue curves), thus confirming that at least in this specific case the hypothesized motion model matches the actual target dynamics. For comparison, Fig. 19
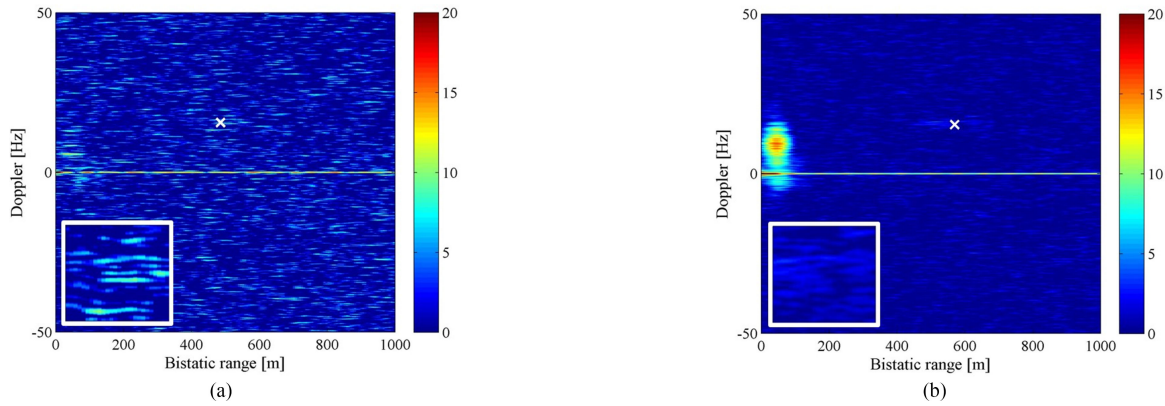
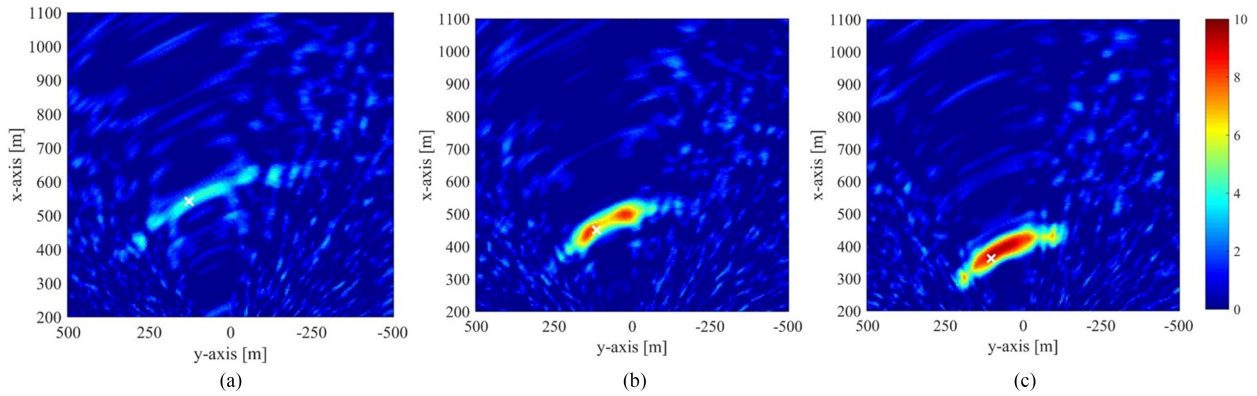Fig. 15. (a) Single RD map (3 s). (b) Integration of 20 RD maps (3 s each) without TMC.

Fig. 16. Experimental local integrated maps over T = 60 s. (a) Start time = 0 s. (b) Start time 30 s. (c) Start time 58 s.
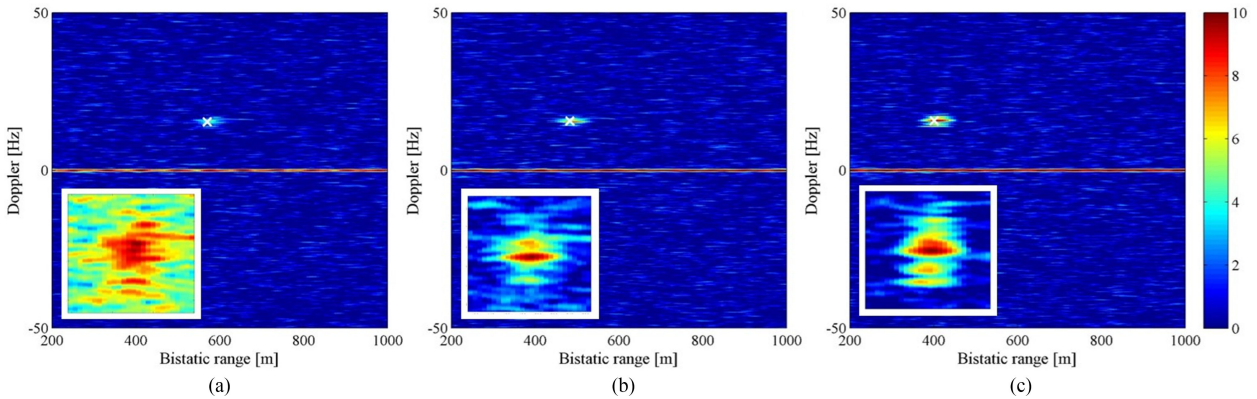

Fig. 17. Experimental RD integrated maps over T = 60 s. (a) Start time = 0 s. (b) Start time 30 s. (c) Start time 58 s.

shows the corresponding *x* and *y* cross sections obtained by applying the local plane based technique. Also in this case there is a good agreement between the results obtained with the proposed technique and the ones exploiting the actual target track information.

Above results confirm the effectiveness of the proposed techniques at collecting the signal energy over long integration times (∼1 min). In order to provide a meaningful quantification of the improvement of the detection performance arising from the exploitation of the proposed long integration time techniques, we evaluated the SNR obtained for an increasing number of aligned and integrated

RD maps. We recall that the noncoherent integration of the correctly aligned (local or RD) maps allows accumulating the target energy over the dwell time, while, in contrast, it reduces the fluctuations of the disturbance contribution. Therefore, for a given number of integrated maps, we define the level of signal to disturbance ratio as

$$\text{SNR} = \frac{P_s - P_n}{\sigma_n} \qquad (22)$$

where P_s is the obtained signal power, P_n and σ_n are, respectively, the mean and the standard deviation of the disturbance background. We considered a set of $N_f = 19$
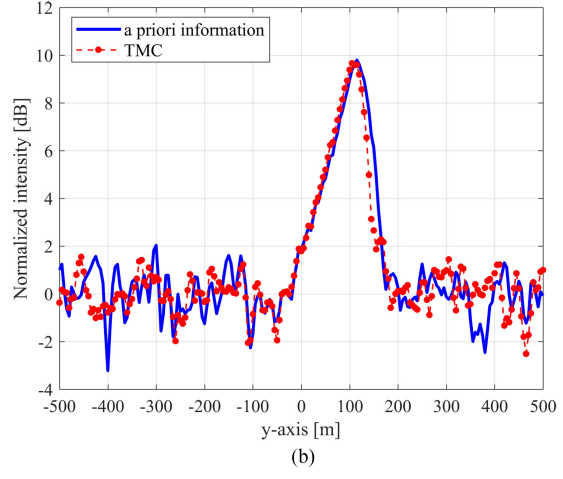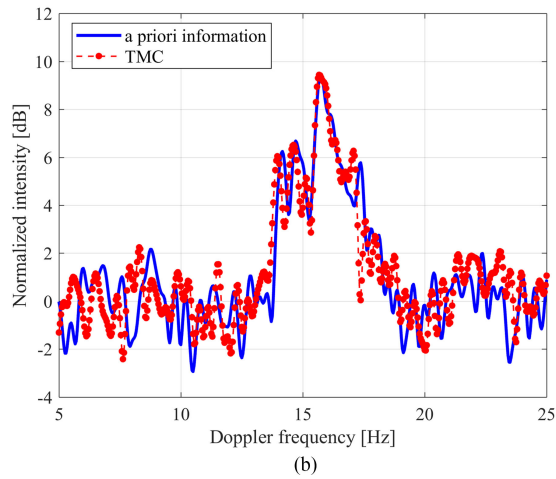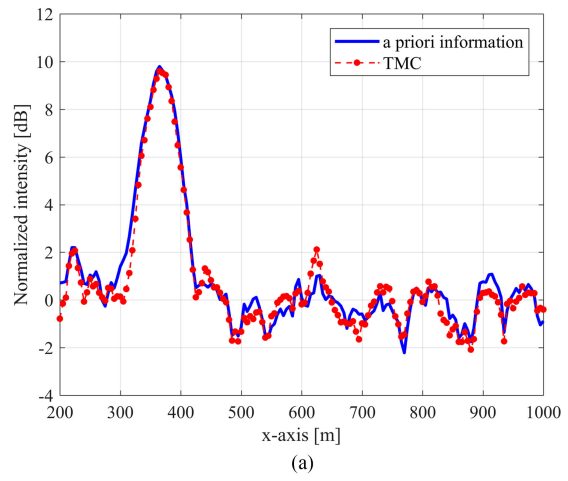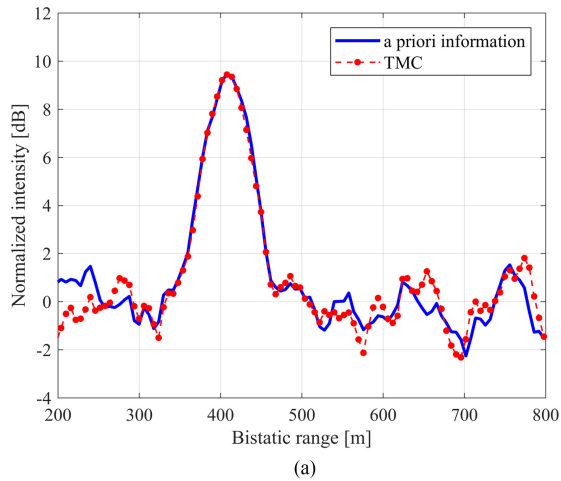
Fig. 18.   Comparison between results obtained with basic plane based technique and GPS measurement at start time 58 s. (a) Bistatic range cuts. (b) Doppler frequency cuts.

Fig. 19.   Comparison between results obtained with the local plane based technique and GPS measurement at start time 58 s. (a) x-axis cuts. (b) y-axis cuts.

compensated maps aligned to the central position of the considered interval. The Doppler rate driving the alignment has been selected as the one providing the maximum signal power in the final integrated maps. Different integrated maps have been then obtained by combining $n_f = 1, 3, \ldots, 19$ maps around the central map. For each value of n_f, P_s has been estimated as the peak power of the range and Doppler cell corresponding to the actual target location as provided by the GPS ground truth, whereas the disturbance statistic has been evaluated by considering a window containing disturbance contributions only. In this analysis, we focus on the part of the target track most far from the receiver, with the target located at a bistatic range of 522 m at the reference position, since it provides the lower input signal power. The blue markers in Fig. 20 represent the estimated SNR as a function of the number of integrated maps. We point out that for $n_f < 5$ it was not possible evaluating the SNR. This is because for those cases, the high fluctuating background mixes up with the target energy, making not straightforward the evaluation of P_s. Therefore, in this specific scenario, we needed the integration of at least five compensated maps to clearly isolate the target from the background. The black dotted curve represents
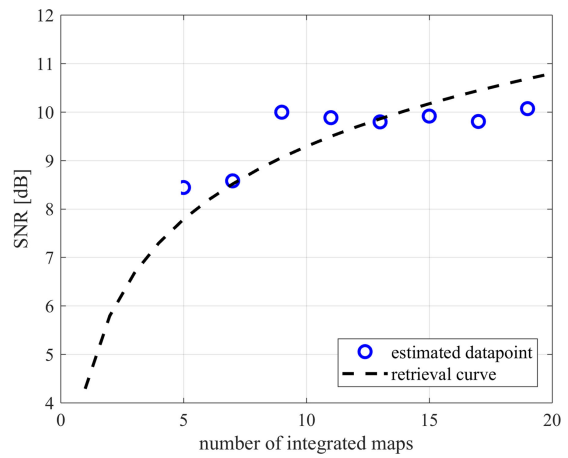

Fig. 20.   Estimated SNR as a function of the number of integrated RD maps.

the retrieved SNR achieved by using in (22) the mean value of P_s (averaged over the different integrated maps where the target was clearly identifiable from the background, $n_f > 5$): the results in the figure allow us to roughly evaluate the improvement of the recovered SNR moving from a single to n_f integrated and properly aligned maps.
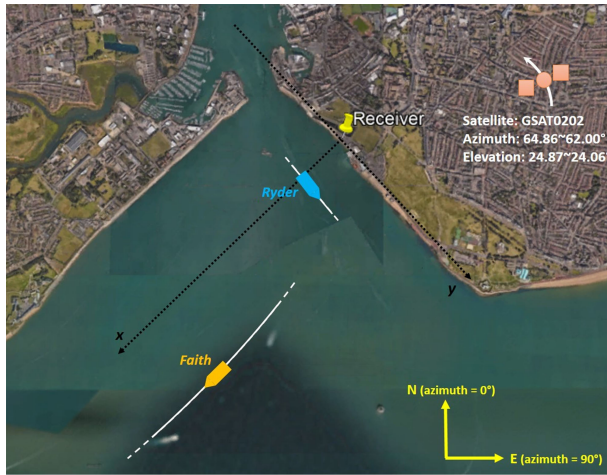
(a)

(b)

(c)

Fig. 21. Second maritime experimental campaign. (a) Acquisition geometry. (b) Noncooperative target "St Faith." (c) Noncooperative target "HSC Wight Ryder I."

TABLE VI
Experimental and Signal Processing Parameters of the Second Maritime Acquisition Campaign

Parameter		Unit	Value
Satellite	number	-	GSAT0202
	carrier frequency	MHz	1176.450
	Chip rate	MHz	10.230
	azimuth (clockwise from N)	deg	$64.86 \sim 62.00$
	elevation (relevant to HC)	deg	$24.87 \sim 24.06$
Processing parameters	sampling frequency	MHz	50
	pulse repetition interval	ms	1
	overall observation interval	s	286
	frame duration	s	3
	non-coherent integrated frames	-	1/5/10/20

B. Experimental Campaign With Opportunity Targets

A second acquisition campaign was conducted near the Portsmouth International port (U.K.). Galileo satellites were exploited as transmitters of opportunity, focusing on the E5a-Q band signal. The receiving hardware was again located on the shore Fig. 21(a). In particular, during the trial, two opportunity targets were in the field of view of the surveillance antenna: the passenger ferry "St Faith" (length: 77.05 m, beam: 17.2 m, draught: 2.48 m) and the catamaran "HSC Wight Ryder I" (length: 41 m, beam: 12 m, draught: 1.60 m), of which optical photographs are shown in Fig. 21(b) and (c), respectively. The real tracks of these vessels were found in the AIS and used as the ground truth for comparison with the experimental results. The experimental and processing parameters are listed in Table VI. Since local and basic plane techniques have been demonstrated to achieve similar performance when the target is

relatively far from the receiver, considering the tracks in Fig. 21(a), only results coming from basic plane approach are reported in the following.

Fig. 22(a) shows the combination of 95 RD maps obtained considering an integration window sliding along the overall observation interval with step of 3 s. Each RD map is obtained by considering $T_f = 3$ s and $N_f = 1$; the combined RD map in Fig. 22(a) is obtained by assigning at each range–Doppler position the highest intensity achieved at that position for all the considered Doppler rate values and integration windows. In this figure, 0 dB represents the background floor evaluated in the final map. As it is apparent, both targets are visible in this map. The near target, "HSC Wight Ryder I, " is at a bistatic range of about 620 m and the far target, "St Faith" in the red frame, is visible until 2656 m. As evident from Fig. 22(a), during the overall acquisition target "St Faith" shows a considerable variation in peak intensity: the main source of this variation is likely due to changes in the target RCS since the involved dynamic range cannot be explained by simply considering the attenuation related to the changing distance.

The target "St Faith, " moving toward the receiver with an almost radial motion, is chosen to demonstrate the capability of long integration time technique to improve the maximum radar range. Fig. 22(b)–(d) show the progressive improvement obtained by applying the basic plane based technique respectively for $N_f = 5$, 10 and 20 and by setting again $T_f = 3$ s. As evident, the maximum detectable range increases with increasing the integration time. As an example, for the case $N_f = 20$ Fig. 23 shows the final map obtained by combining the detection maps corresponding to the different integration windows. Each detection map was obtained by applying to each integrated map provided by the bank (see Fig. 6) a 2D-CA-CFAR detector and by cascading a clustering stage for ambiguous detections removal. As it is apparent, the bright returns visible in Fig. 22(d) correspond to a track in Fig. 23 in good agreement with the ground truth provided by AIS.

To quantify the performance improvement achievable by increasing the integration window, Table VII lists the maximum radar range at which the target is detected for
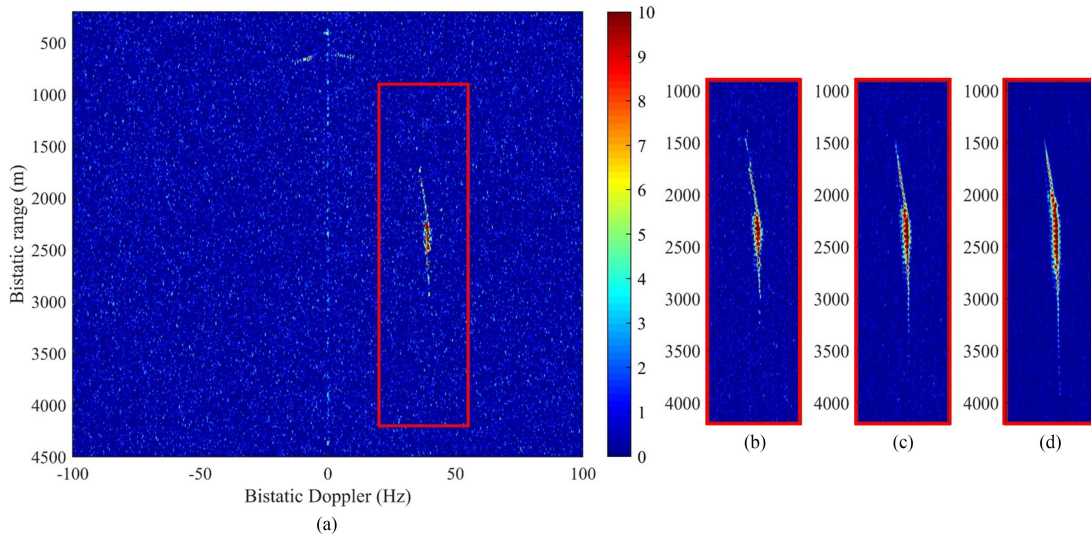
Fig. 22. RD tracks concerning the target "St Faith" over 286 s dwell time. (a) $N_b = 1$. (b) $N_b = 5$. (c) $N_b = 10$. (d) $N_b = 20$.

TABLE VII
Maximum Radar Range

|	$N_f = 1$	$N_f = 5$	$N_f = 10$	$N_f = 20$
Maximum Range $R_{max}(N_f)$, [m]	2656 ($u_{N_f=1}$=155 sec)	2986 ($u_{N_f=5}$=122 sec)	3310 ($u_{N_f=10}$=89 sec)	3915 ($u_{N_f=20}$=30 sec)
Experimental Maximum Range Gain $\left[R_{max}(N_f)/R_{max}(N_f=1)\right]^2$, [dB]	-	1.1	1.9	3.4
Experimental RCS variation $\sigma\left(u_{N_f=1}\right)/\sigma\left(u_{N_f}\right)$, [dB]	-	5.7	7.9	7.3
Experimental Integration Gain $I_{exp}(N_f) = \left[R_{max}(N_f)/R_{max}(N_f=1)\right]^2 \cdot \sigma\left(u_{N_f=1}\right)/\sigma\left(u_{N_f}\right)$, [dB]	-	6.7	9.8	10.7
Theoretical Integration Gain $I(N_f)$, eq. (4), [dB]	-	5.6	7.7	9.7
Theoretical Integration Gain Interval $\left[\sqrt{N_f},\ N_f\right]$, [dB]		[3.5, 7]	[5, 10]	[6.5, 13]
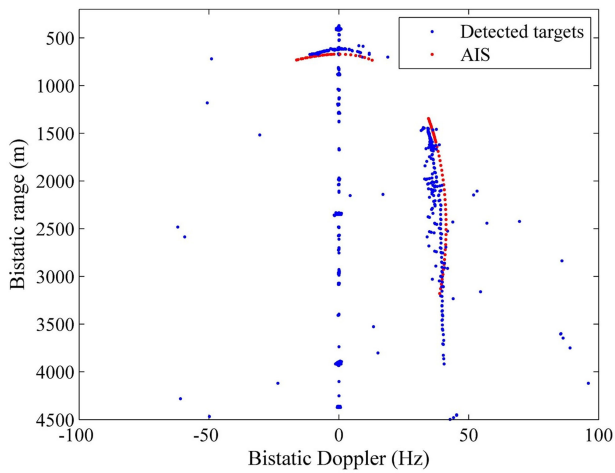
Fig. 23. Final detection map by applying CA-CFAR detector ($N_f = 20$).

the considered cases (having set $P_{fa} = 10^{-3}$). Particularly, these values are defined as the starting point from which the target track is observable with continuity. In the same tables are also reported:

1) The experimental integration gain measured from maximum radar range improvement as the squared value of the ratio of maximum range when $N_f > 1$ to maximum range when $N_f = 1$.

2) The experimental RCS variation measured between slow time instant when target is at the maximum range concerning case $N_f = 1$ and slow time instant when target is at the maximum range concerning $N_f > 1$: In evaluating this quantity a normalization has been applied taking into account the different attenuations related to the different range values. As apparent from results in the table (and also from images in Fig. 22), target RCS shows a considerable variation with increasing values as slow time increases.

3) The experimental overall integration gain obtained as the combination of the two above components.

4) The theoretical integration gain value as from (4) and, as a more relaxed reference, a possible interval of values between $\sqrt{N_f}$ and N_f.

From shown results, it is possible to observe that the experimental overall integration gain is well in line with theoretical predictions: particularly, part of the integration

gain available when increasing N_f is used to compensate the loss in RCS observed in this particular acquisition and part is exploited for the maximum radar range improvement. A higher maximum range improvement could be achieved for those cases involving a more stable RCS value. Noticeably, target "St Faith" is detected up to 4 km. Furthermore, performance improvement could be obtained by exploiting multiple transmitters, which will be the subject of future work.

VI. CONCLUSION

In this paper, we have exploited the potential of using GNSS as transmitters of opportunity for maritime surveillance applications. The global coverage offered by GNSS satellites makes them extremely appealing as gap fillers for those areas that cannot be reached by terrestrial transmissions such as the open sea. Particularly, here the focus has been on the definition of suitable techniques able to properly integrate the returns from moving targets over long dwell times in order to counteract the low power density of the transmitted signal reaching the ground level, which represents the fundamental bottleneck of this technology for target detection.

To this purpose, two different processing techniques have been proposed and their performance analyzed and compared: The first one works in the local plane representing the ground plane surrounding the receiver and, if fed with the right motion model, performs as an optimum integration of the target contributions; the second one operates in the basic range–Doppler plane under the assumption of a linear Doppler history, thus being a suboptimum solution in terms of achievable integration gain but more efficient from a computational point of view. For both approaches proper filter banks have been proposed to match the specific unknown target motion condition and the required design criteria provided. The two techniques have been preliminarily tested against synthetic data: shown results demonstrate that in many practical applications the two techniques are equivalent in terms of integration gain; some losses of the basic plane based technique with respect to the local plane based approach are experienced only for those targets moving at high speed at short range where the linear approximation for the Doppler history does not suffice. Then, results from two experimental trials have been reported and discussed to show the relative improvement in SNR and detection range provided by the integration over long dwell time. The first trial (using GLONASS transmitter) involved a small cooperative fishing boat equipped with GPS: obtained results clearly demonstrate the need to integrate over long time intervals (some tens of seconds) to detect small targets and, for the integration to be effective, to properly compensate the target motion, and the effectiveness and almost equivalence, in terms of integration gain, of the two approaches and their capability of adapting to the unknown motion conditions. The second trial (exploiting Galileo transmissions) involved opportunity targets with reference ground truth provided by AIS receiver: obtained results demonstrated the achievement of an experimental integration gain well in line with theoretical predictions, thus proving the effectiveness of the proposed approaches in practical applications.

Finally, it is worth to remark that one of the bigger benefits arising from the use of GNSS is the multitude of transmitters simultaneously illuminating the same area. Even though the case of a single transmitter has been here considered, it makes sense that the exploitation of multiple sources can greatly increase the performance of the proposed system, and this will be the focus of future work.

ACKNOWLEDGMENT

REFERENCES

[1] R. Zemmari, M. Broetje, G. Battistello, and U. Nickel
GSM passive coherent location system: Performance prediction and measurement evaluation
IET Radar Sonar Navig., vol. 8, no. 2, pp. 94–105, Feb. 2014.

[2] K. Chetty, K. Woodbridge, H. Gui, and G. E. Smith
Passive bistatic WiMAX radar for marine surveillance
In *Proc. IEEE Int. Radar Conf.*, Washington, DC, USA, May 2010, pp. 188–193.

[3] F. Colone, D. Langellotti, and P. Lombardo
DVB-T signal ambiguity function control for passive radars
IEEE Trans. Aerosp. Electron. Syst., vol. 50, no. 1, pp. 329–347, Jan. 2014.

[4] *Navstar IS-GPS-200E, Interface Specification*, Science Applications International Corporation, El Segundo, CA, USA, Tech. Rep. IRN-IS-200H-003, Dec. 2015.

[5] *Global Navigation Satellite System GLONASS Interface Control Document (Edition 5.1)*, Russian Institute of Space Device Engineering, Nizhnyaya Salda, Russia, 2008.

[6] *BeiDou Navigation Satellite System Signal in Space Interface Control Document, Open Service Signal (Version 2.0)*, China Satellite Navigation Office, Beijing, China, Dec. 2013.

[7] *Galileo Open Service, Signal in Space Interface Control Document (OS SIS ICD)*, European Space Agency/European GNSS, Paris, France, Nov. 2015.

[8] M. Martín-Neira
A passive reflectometry and interferometry system (PARIS): Application to ocean altimetry
ESA J., vol. 17, pp. 331–355, 1993.

[9] S. Jin, G. P. Feng, and S. Gleason
Remote sensing using GNSS signals: Current status and future directions
J. Adv. Space Res., vol. 47, pp. 1645–1653, 2011.

[10] V. U. Zavorotny, S. Gleason, E. Cardellach, and A. Camps
Tutorial on remote sensing using GNSS bistatic radar of opportunity
IEEE Geosci. Remote Sens. Mag., vol. 2, no. 4, pp. 8–45, Dec. 2014.

[11] M. Cherniakov and T. Zeng
Passive bistatic SAR with GNSS transmitters
In *Bistatic Radar: Emerging Technology*, M. Cherniakov, Ed. New York, NY, USA: Wiley, 2008.

[12] M. Antoniou and M. Cherniakov
GNSS-based bistatic SAR: A signal processing view
EURASIP J. Adv. Signal Process., 2013, Art. no. 98.

[13] M. Antoniou, Z. Zeng, L. Feifeng, and M. Cherniakov
Experimental demonstration of passive BSAR imaging using
navigation satellites and a fixed receiver
IEEE Geosci. Remote Sens. Lett., vol. 9, no. 3, pp. 477–481,
May 2012.

[14] M. Antoniou, Z. Hong, Z. Zhangfan, R. Zuo, Q. Zhang, and
M. Cherniakov
Passive bistatic synthetic aperture radar imaging with Galileo
transmitters and a moving receiver: Experimental demonstra-
tion
IET Radar Sonar Nav., vol. 7, no. 9, pp. 985–993, Dec. 2013.

[15] Q. Zhang, M. Antoniou, W. Chang, and M. Cherniakov
Spatial decorrelation in GNSS-based SAR coherent change
detection
IEEE Trans. Geosci. Remote Sens., vol. 53, no. 1, pp. 219–228,
Jan. 2015.

[16] F. Santi, M. Antoniou, and D. Pastina
Point spread function analysis for GNSS-based multistatic SAR
IEEE Geosci. Remote Sens. Lett., vol. 12, no. 2, pp. 304–308,
Feb. 2015.

[17] H. Ma, M. Antoniou, and M. Cherniakov
Passive GNSS-based SAR resolution improvement using joint
Galileo E5 signals
IEEE Geosci. Remote Sens. Lett., vol. 12, no. 8, pp. 1640–1644,
Aug. 2015.

[18] F. Santi, M. Bucciarelli, D. Pastina, M. Antoniou, and M. Cherni-
akov
Spatial resolution improvement in GNSS-based SAR using
multistatic acquisitions and feature extraction
IEEE Trans. Geosci. Remote Sens., vol. 54, no. 10, pp. 6217–
6231, Oct. 2016.

[19] E. P. Glennon, A. G. Dempster, and C. Rizos
Feasibility of air target detection using GPS as a bistatic radar
J. Global Positioning Syst., vol. 5, no. 1–2, pp. 119–126, 2006.

[20] I. Suberviola, I. Mayordomo, and J. Mendizabal
Experimental results of air target detection with a GPS forward-
scattering radar
IEEE Geosci. Remote Sens. Lett., vol. 9, no. 1, pp. 47–51,
Jan. 2012.

[21] S. Wachtl, V. Koch, and L.-P. Schmidt
Global navigation satellite systems in passive surveillance
applications
In *Proc. Tyrrhenian Int. Workshop Dig. Commun. Enhanced
Surveillance Aircraft Veh.*, Rome, Italy, 2014, pp. 135–140.

[22] A. Di Simone, H. Park, D. Riccio, and A. Camps
Sea target detection using spaceborne GNSS-R delay-Doppler
maps: Theory and experimental proof of concept using TDS-1
data
IEEE J. Sel. Topics Appl. Earth Obs. Remote Sens., vol. 10,
no. 9, pp. 4237–4255, Sep. 2017.

[23] M.-P. Clarizia, P. Braca, C. S. Ruf, and P. Willet
Target detection using GPS signals of opportunity
In *Proc. 18th Int. Conf. Inf. Fusion*, 2015, pp. 1429–1436.

[24] A. K. Brown
Remote sensing using bistatic GPS and digital beam-steering
receiver
In *Proc. Int. Geosci. Remote Sens. Symp.*, 2005, vol. 1, pp. 416–
419.

[25] H. Ma *et al.*
Maritime target detection using GNSS-based radar: Experimen-
tal proof of concept
In *Proc. IEEE Radar Conf.*, Seattle, WA, USA, May 2017,
pp. 0464–0469.

[26] F. Pieralice *et al.*
GNSS-based passive radar for maritime surveillance: Long in-
tegration time MTI technique
In *Proc. IEEE Radar Conf.*, Seattle, WA, USA, May 2017,
pp. 0508–0513.

[27] H. Ma *et al.*
Maritime moving target indication using passive GNSS-based
bistatic radar
IEEE Trans. Aerosp. Electron. Syst., vol. 54, no. 1, pp. 115–130,
Feb. 2018.

[28] X. He, M. Cherniakov, and T. Zeng
Signal detectability in SS-BSAR with GNSS non-cooperative
transmitter
IEE Proc. Radar, Sonar Navig., vol. 152, no. 3, pp. 124–132,
Jun. 2005.

[29] J. Xu, J. Yu, Y.-N. Peng, and X.-G. Xia
Radon-fourier transform for radar target detection, I: General-
ized doppler filter bank
IEEE Trans. Aerosp. Electron. Syst., vol. 47, no. 2, pp. 1186–
1202, Apr. 2011.

[30] X. Chen, J. Guan, N. Liu, and Y. He
Maneuvering target detection via radon-fractional Fourier
transform-based long-time coherent integration
IEEE Trans. Signal Process., vol. 62, no. 4, pp. 939–953,
Feb. 2014.

[31] K. Kulpa and J. Misiurewicz
Stretch processing for long integration time passive covert radar
In *Proc. CIE Int. Conf. Radar*, Shanghai, China, 2006, pp. 1–4.

[32] Z. Li, F. Santi, D. Pastina, and P. Lombardo
Multi-frame fractional Fourier transform technique for moving
target detection with space-based passive radar
IET Radar Sonar Navig., vol. 11, no. 5, pp. 822–828, May
2017.

[33] F. Santi, D. Pastina, and M. Bucciarelli
Maritime moving target detection technique for passive bistatic
radar with GNSS transmitters
In *Proc. Int. Radar Symp.*, Prague, Czech Republic, Jun. 28–
30, 2017, pp. 1–10.

[34] P. Z. Peebles Jr.
Radar Principles. New York, NY, USA: Wiley, 1998.

[35] W. J. Albersheim
A closed-form approximation to Robertson's detection
characteristics
Proc. IEEE, vol. 69, no. 7, p. 839, Jul. 1981.

[36] T. Kelso
CelesTrak
Public domain satellite tracking data, 2010. [Online].
Available: http://celestrak.com/

[37] F. Colone, D. W. O'Hagan, P. Lombardo, and C. J. Baker
A multistage processing algorithm for disturbance removal and
target detection in passive bistatic radar
IEEE Trans. Aerosp. Elect. Syst., vol. 45, no. 2, pp. 698–722,
Apr. 2009.

Debora Pastina (M'01) received the Laurea degree in telecommunications engineering and the Ph.D. degree in information and telecommunications engineering from Sapienza University of Rome, Rome, Italy, in 1996 and 2000, respectively.

From July 1998 to March 1999, she carried on research activity with the SAR Processing Team, Defence Evaluation Research Agency, Malvern, U.K. She is currently an Assistant Professor with the DIET Department, Sapienza University of Rome. She is involved and is responsible of scientific research projects funded by the Italian Ministry of Research, the Italian Space Agency, the European Commission, and the national radar industry. The results of her activity have been reported in more than 100 journal and conference papers. Her main research interests include SAR/ISAR, GMTI techniques, GNSS-based passive radar systems, FSR systems, clutter models, radar detection in non-Gaussian clutter.

Dr. Pastina was the Chairman of the Local Committee of the IEEE/ISPRS Joint Workshop Urban 2001. She was the Publication Chair of the 2008 IEEE Radar Conference. She is a member of the Editorial Board of the *International Journal of Electronics and Communications* (AEÜ, Elsevier) and of the IEEE TRANSACTIONS ON AEROSPACE AND ELECTRONIC SYSTEMS.

Fabrizio Santi (M'15) received the Master's degree (*cum laude*) in telecommunication engineering and the Ph.D. degree in remote sensing from Sapienza University of Rome, Rome, Italy, in September 2010 and June 2014, respectively.

From April to September 2013, he carried on research activity in the Microwave Integrated Systems Laboratory, University of Birmingham, U.K. He is currently a Postdoctoral Researcher with the Department of Information Engineering, Electronics and Telecommunications, Sapienza University of Rome. The results of his research activity have been reported in a number of journals and conference papers. His main research interests include SAR/ISAR radar imaging and space-based active and passive radar systems.

Dr. Santi is a Reviewer for the IEEE TRANSACTIONS ON AEROSPACE AND ELECTRONIC SYSTEMS and other international technical journals. He was the recipient of the Best Italian Thesis on Remote Sensing Award from the IEEE Geoscience and Remote Sensing South Italy.

Federica Pieralice was born in Rome, Italy, in May 1988. She received the Bachelor's degree in aerospace engineering and the Master's degree in space engineering with a thesis on change detection technique for multitemporal SAR images from Sapienza University of Rome, Rome, Italy, in December 2011 and May 2015, respectively. She is currently working toward the Ph.D. degree in radar and remote sensing at the Department of Information Engineering, Electronics and Telecommunications, Sapienza University of Rome.

Her current research interest focuses on passive radar systems based on GNSS for maritime surveillance applications. Throughout her Ph.D., she is involved in the Horizon 2020 Research Project "Galileo-based passive radar system for maritime surveillance (spyGLASS)."

Marta Bucciarelli received the Laurea degree in communication engineering and the Ph.D. degree in radar and remote sensing from Sapienza University of Rome, Rome, Italy, in 2006 and 2010, respectively.

In 2010, she received a four-year contract with the DIET Department Sapienza University of Rome. In 2014, she was with the NATO STO CMRE as a Visiting Researcher. She actually works for the academic spinoff Sympas S.r.l, which she cofounded in 2009. She has been and is involved in scientific research projects funded by the European Commission, the Italian Space Agency, the Italian Ministry of Research and the Italian industry. Her current research interests include multichannel active, passive, multistatic and MIMO high-resolution ISAR imaging, adaptive multichannel signal processing, and GNSS-based passive radar systems.

Dr. Bucciarelli is a Reviewer for international journals, conferences, and scientific books.
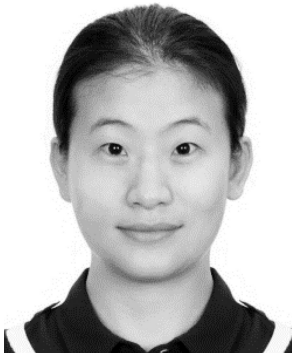
Hui Ma was born in Hebei, China, in Octobor 1989. She received the B.Sc. degrees in electronic and information engineering in July 2009 and the Ph.D. degree in electromagnetics and microwave technology in July 2015 from the Beihang University, Beijing, China.

From November 2012 to November 2014, she was as a visiting Ph.D. student with the University of Birmingham, Birmingham, U.K., where she continued as a Research Fellow from November 2015 to May 2017, under the grants funded by the European Space Agency. Since June 2017, she has been a Lecturer with the National Laboratory of Radar Signal Processing, Xidian University, Xi'an, China. Her research interests include radar imaging, MIMO radar, passive radar, and radar signal processing.

Dr. Ma is a Reviewer for the IEEE Transaction ON AEROSPACE AND ELECTRONIC SYSTEMS, GPS Solutions, and other international technical journals.

Dimitrios Tzagkas completed the studies on physics and received the Master's degree in electronic engineering and communication engineering from the Aristotle University of Thessaloniki, Thessaloniki, Greece, and the Ph.D. degree on Passive SAR in the Microwave Integrated Systems Laboratory, University of Birmingham, Birmingham, U.K.

He continued his Postdoctoral Researcher with Microwave Integrated Systems Laboratory, University of Birmingham. The results of his research activity can be found in a number of publications on Passive Radar applications.

Michail Antoniou received the B.Eng.(Hons.) degree in electronic and communications engineering and the Ph.D. degree in radar sensors and systems from the University of Birmingham, Birmingham, U.K., in 2003 and 2007, respectively.

From 2006 to 2011, he was a Research Fellow with the Microwave Integrated Systems Laboratory, University of Birmingham. Since 2011, he has been with the Department of Electronic, Electrical, and Systems Engineering, University of Birmingham, where he is currently a Senior Lecturer. He leads a team of researchers on radar systems and signal processing, including Synthetic Aperture Radar (SAR), bi-/multistatic radar, passive radar, MIMO, and cognitive/bioinspired radar.

Dr. Antoniou has more than 70 publications in peer reviewed international journals and conferences, and he has led research grants funded by the European Commission, the European Space Agency, the U.K. MoD and the British Council, as well as direct industrial grants in this area.

Mikhail Cherniakov received the M.Eng. in electronic systems the Ph.D. degree in radar signal processing, and the D.Sc. degree in microwave systems from the Moscow Institute of Electronics Engineering (MIEE), Moscow, Russia, in 1974, 1980, and 1992, respectively.

He is a Professor with the Aerospace and Electronic Systems, University of Birmingham, Birmingham, U.K. In 1981, he became the founding Head of the Microwave Systems R&D Laboratory. In 1992, he accepted an appointment as Professor with the MIEE. From 1995, he held a post with the Department of Information Technology and Electrical Engineering, University of Queensland, St Lucia, QLD, Australia. He was with the School of EECE, University of Birmingham, in 2000 and is the head of the Microwave Integrated Systems Laboratory. The area of his research activity is radar technology. He is the author of more than 300 papers, patents and three books.

Dr. Cherniakov was awarded by Christian Hülsmeyer prize, in 2017.